This document was prepared for the ETI by third parties under contract to the ETI. The ETI is making these documents and data available to the public to inform the debate on low carbon energy innovation and deployment.

Programme Area: Marine

Project: PerAWAT

Title: Report on Model Setup for Horizontal Axis Axial Flow Turbines

Abstract:

The testing programme devised for producing validation data for the assessment of numerical models of large arrays has been successfully completed. In the process of completing this test programme new methodologies for the testing of WEC arrays have been developed that support the isolation of array interactions from other physical testing artefacts as well as enabling the uncertainty in WEC performance to be estimated. This is considered to be a significant addition to the outcome of this testing programme that will have a major impact on the design of wave tank testing of WEC arrays. Although in general the data quality is high, in the characterisation testing it is lower than desired due to unresolved resonant oscillations in the supporting structure, which was evident to some extent in all the characterisation tests. However, the characterisation testing is not considered to be a critical element of the test programme and has a minimal impact on the extent of validation data produced.

Context:

The Performance Assessment of Wave and Tidal Array Systems (PerAWaT) project, launched in October 2009 with £8m of ETI investment. The project delivered validated, commercial software tools capable of significantly reducing the levels of uncertainty associated with predicting the energy yield of major wave and tidal stream energy arrays. It also produced information that will help reduce commercial risk of future large scale wave and tidal array developments.

Energy Technologies Institute

PerAWaT

WG3 WP1 D1: REPORT ON MODEL SETUP FOR HORIZONTAL AXIS AXIAL FLOW TURBINES

Authors S. C. McIntosh, C. Fleming, R.H.J. Willden

Version 2.0

Date 5th November 2010

Revision History		
Issue / Version	Issue Date	Summary
0.1	29/10/10	Early draft Submitted to GH
0.2	03/11/10	Completed draft submitted to GH
1.0	05/11/10	Updated following comments by GH
2.0	20/12/10	Updated following comments by ETI

Executive summary

This report describes the model setup for a flume scale horizontal axial flow tidal turbine; forming the first deliverable of Work Group 3, Work Package 1 WG3 WP1 D1. Undertaken at the University of Oxford, this numerical work is complemented by an experimental program carried out by EDF under WG4 WP1.

Close collaboration between EDF and the University of Oxford has ensured that both sets of experiments are conducted using fluid-dynamically similar geometries operating within a clearly defined flow environment to aid future comparisons planned for WG3 WP1 D3.

A demonstration of model validity is undertaken for both the hydrodynamic environment (velocity profile, turbulence intensities, turbulent length scales, local free-surface height) and the rotor assembly. Verification is performed on a component-by-component basis with comparison to experimental data wherever possible.

Bare flume simulations compare well with EDF's base-line flow measurements for the low velocity, low turbulence intensity case *U0, T0* informing numerical inflow conditions. An unexplained centre-line velocity dip occurring at higher flow speeds, *U1,* and turbulence intensities, *T1,* in the experimental data-set has delayed numerical verification utilising the higher turbulence intensity case. The implementation of a free-surface capture scheme is shown to function well with excellent agreement with a number of theoretical test cases shown.

Three-dimensional aerofoil simulations of a constant chord section of the rotor blade demonstrate grid convergence for this critical model component. Force predictions are shown to compare well to wind tunnel data. The support tower is also shown to be adequately represented in the numerical model.

Finally, a full three-dimensional simulation of the rotor assembly operating within the EDF flume at a tip-speed-ratio of λ=3.5 is presented highlighting a number of pertinent flow features.

Table of contents

1 Introduction

Work described within this report is carried out within the PerAWaT project as part of Work Group three, Work Package one, Deliverable one WG3WP1D1. Numerical simulations on device-scale, array-scale and basin-scale tidal energy conversion all fall within WG3. The primary concern of this work package is the development of numerical models capable of accurately simulating the flow physics of single tidal devices operating under various environmental influences. Furthermore, the work package aims to use numerical simulation of stand-alone devices operating within realistic flow conditions to better establish single device performance and wake structure when deployed in open water conditions.

The performance of three generic Fundamental Device Concepts (FDCs) are investigated within the project as a whole; bare, ducted and open centre axial flow turbines. Bare turbines are investigated numerically both in this work package and also that being undertaken by the University of Edinburgh, WG3 WP5. Ducted turbines will be considered at Oxford, and open centre devices at Edinburgh.

Work done by the University of Oxford within WG3 will, in the case of bare turbines, encompass both model and full-scale devices and hence serve as a numerical link between the bare turbine lab-scale experiments conducted by EDF as part of WG4 WP1 and the full-scale tidal turbine hydrodynamics being simulated by Oxford and Edinburgh.

Within this work package, turbine flows are simulated through solution of the governing unsteady three-dimensional equations of motion. Conservation of mass and momentum equations are solved in a Reynolds averaged form along with associated turbulence closure models using a commercially available Computational Fluid Dynamics solver, FLUENT. Provision for multi-phase flows, necessary to resolve the water-air interface, are appended to the FLUENT environment in the form of User Defined Functions UDFs.

This report forms D1, and describes the numerical model of a model-scale bare horizontal axis turbine operating within an experimental flume.

The hydrodynamic environment of the experimental flume facility is first analyzed forming the base-line bare-flume flow-field in Section 2.1. This base-line flow-field map is then used to develop numerical models of the bare flume in Section 2.2. The inclusion of an air-water interface above the bare-flume flow-field is subsequently introduced in Section 2.3.

Development and verification of the rotor model is the primary focus of Section 3. Here a component-by-component verification of each fluid-dynamically significant part is performed including validation with experiment wherever possible.

Finally, in Section 4, a full composite simulation is developed, and analysis is carried out on the resulting flow field.

2 The Hydrodynamic Environment

The performance of axial flow turbines is strongly affected by the environment within which they operate. Variations in velocity shear, free-surface proximity and the length scales and intensities of the associated turbulent flows can significantly impact both turbine integral quantities (power and thrust) and wake development.

Work undertaken within WG3 WP1 (numerical) and WG4 WP1 (experimental) aims to quantify, and cross-validate, the influence of a generic tidal environment on rotor performance and wake structure. For this cross-validation to take place it is vital that investigations are carried out under the same baseline conditions.

2.1 Base-line Flow-field

A series of 'base-flow' mapping investigations have been carried out by EDF to quantify the experimental environment and to inform the numerical work. Velocity grid data from the base-flow maps for a reference flow velocity *U0* and turbulence intensities *T0* and *T1* are presented and discussed. The *T0* ('clean' floor) environment corresponds to the natural state within the flume, whilst *T1* (breezeblock) corresponds to a higher turbulence intensity state that is induced through increased flume wall roughness (due to breezeblocks). Special

consideration is given to the impact of the turbulence production technique on the time-averaged flow-field for the *T1* case.

2.1.1 Experimental Setup

An illustrative schematic of the EDF flume identifying the stream-wise location of the rotor (or measurement) plane and the position of breezeblock roughness elements for the *T1* case is shown in Figure 2.1.1. Three component velocity signals recorded over a 13x8 grid of width *1.1*m and height 0.*65*m, roughly centrally located within the measurement plane, have been provided to Oxford by EDF. Each velocity signal is sampled at a frequency of *25*Hz over a ~*120*s period. Baseline cases with a reference velocity of *U0=0.27*ms^{-1} and turbulence intensities of *T0* and *T1* are discussed below.

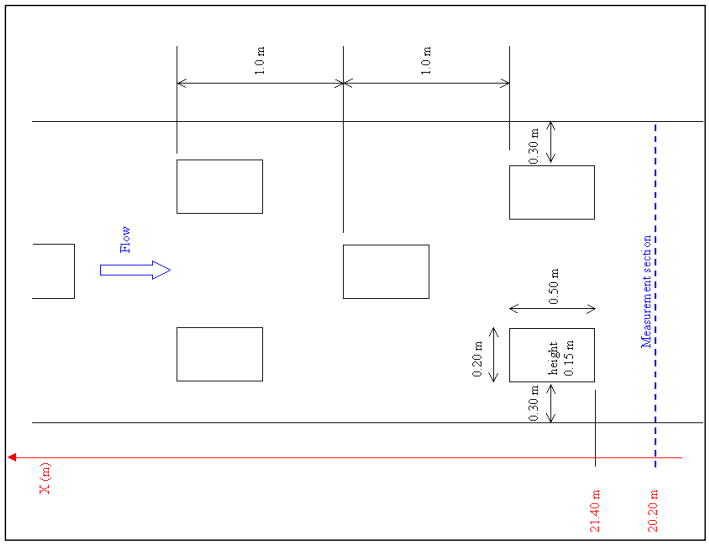

Figure 2.1.1: Distribution of roughness elements in flume (*T1*); figure provided by EDF.

A right-handed coordinate system aligned with the stream-wise flow (x) and vertical height (z) is employed to process and communicate the baseline flow maps.

2.1.2 Velocity Grid Analysis

The raw velocity signals are processed into: time averaged velocity,

$$\overline{\mathbf{u}} = \frac{1}{T}\int_0^T \mathbf{u}\, dt, \qquad \textbf{(2.1)}$$

turbulence intensity,

$$TI = \frac{\left(\frac{1}{T}\int_0^T \left((u-\bar{u})^2 + (v-\bar{v})^2 + (w-\bar{w})^2\right) dt\right)^{\frac{1}{2}}}{|\bar{\mathbf{u}}|}, \quad \textbf{(2.2)}$$

and vorticity,

$$\omega = \nabla \times \mathbf{u}. \quad \textbf{(2.3)}$$

where T is a long time period in relation to that of the turbulent velocity fluctuations.

The flow environment for the low turbulence intensity case *T0* is shown in Figure 2.1.2. The turbine plane grid data is presented as would be observed looking down the flume in the stream-wise direction. The position of the flume walls / mean water surface is indicated by solid black lines and the position of the rotor by a dash-dot black line.

The presence of wall boundary layers extending from both the flume's floor and sides is clearly visible in the mean stream-wise velocity grid shown in Figure 2.1.2a. Here, velocity contours form an approximately 'U' shaped topology with broadly similar horizontal and vertical profiles indicating a comparable mean wall roughness between the flume's floor and sidewalls. Beyond these layers a 'core' flow of roughly constant velocity is present, occupying the upper half of the rotor's swept area. Figure 2.1.2b illustrates regions of increased unsteadiness with $TI \sim 10\%$ close to the flume's walls dropping to a relatively low value of $TI \sim 5\%$ within the velocity 'core'. Stream-wise vorticity is shown in Figure 2.1.2c to remain relatively low across the grid with peak values present close to the flume's walls.

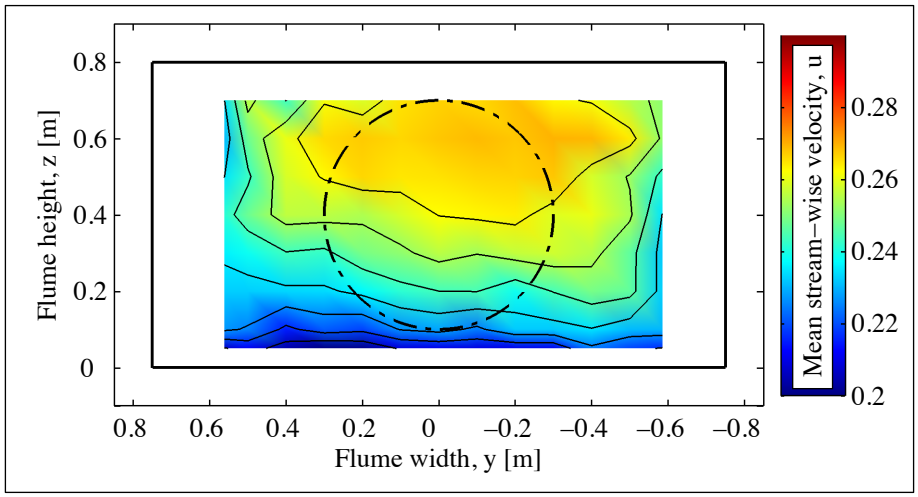

a. Mean stream-wise velocity, u [ms^{-1}].

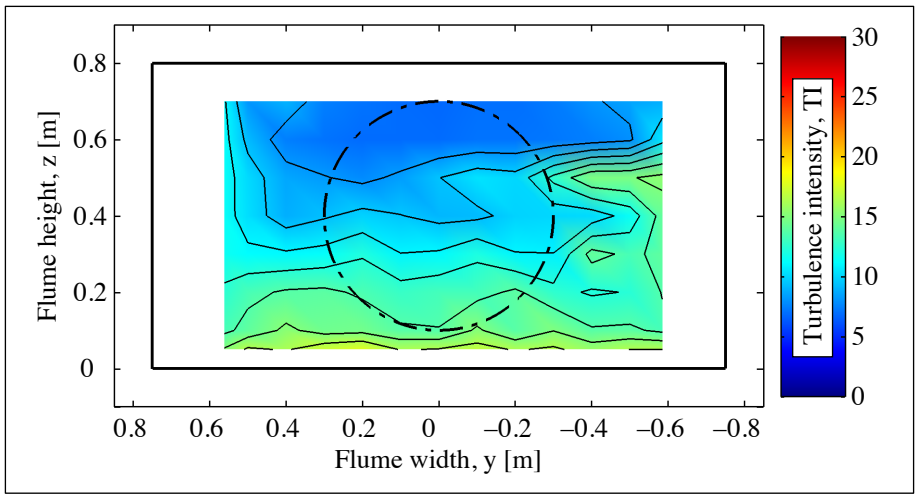

b. Turbulence intensity, TI [%].

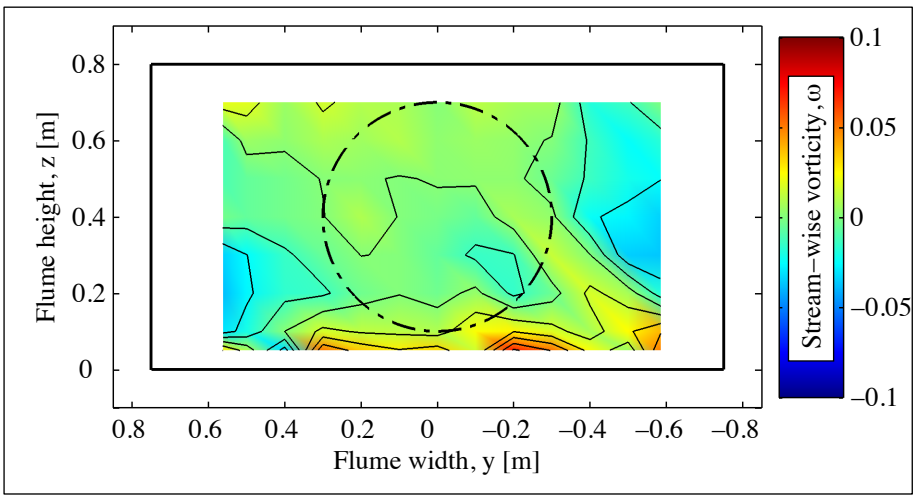

c. Stream-wise vorticity, ω_x [s^{-1}].

Figure 2.1.2: Low turbulence intensity turbine plane measurement grid (*U0, T0*).

The high turbulence intensity case *T1* is presented in Figure 2.1.3. In addition to the location of flume walls and turbine, the stream-wise area occupied by the breezeblock roughness elements, shown schematically in Figure 2.1.1, is illustrated by translucent grey elements spaced along the flume's floor.

The impact of increased floor roughness is clearly visible in Figure 2.1.3a, with the mean stream-wise velocity profile indicating a floor boundary layer of greatly increased thickness with respect to the flume sides. The addition of roughness elements is also shown to produce a significant deficit in the mean stream-wise velocity field close to the flume's centerline in the bottom half of the water column that is not present in the *T0* flow. This asymmetry applied across the rotor's cross-stream width would be unlikely to occur in real tidal flows and is thus considered an undesirable characteristic of the *T1* environment. Figure 2.1.3b illustrates a region of increased turbulence intensity corresponding to the dip in centerline velocity; indicating increased levels of shear in this area. Also present in the turbulence intensity plot of Figure 2.1.3b, and to a lesser extent in Figure 2.1.2b, is a wedge of increased turbulence intensity protruding from the right hand wall (y=-0.55m, z=0.5m). The production mechanism for this flow irregularity is not known.

The cause of the decreased centerline velocity and cross-stream non-uniformity can be explained by the presence of a number of stream-wise vortical structures imbedded within the mean flow-field (Figure 2.1.3c). Here, each breezeblock can be seen to shed a pair of strong, persistent, oppositely signed vorticies aligned with the stream-wise flow and impacting on the turbine plane.

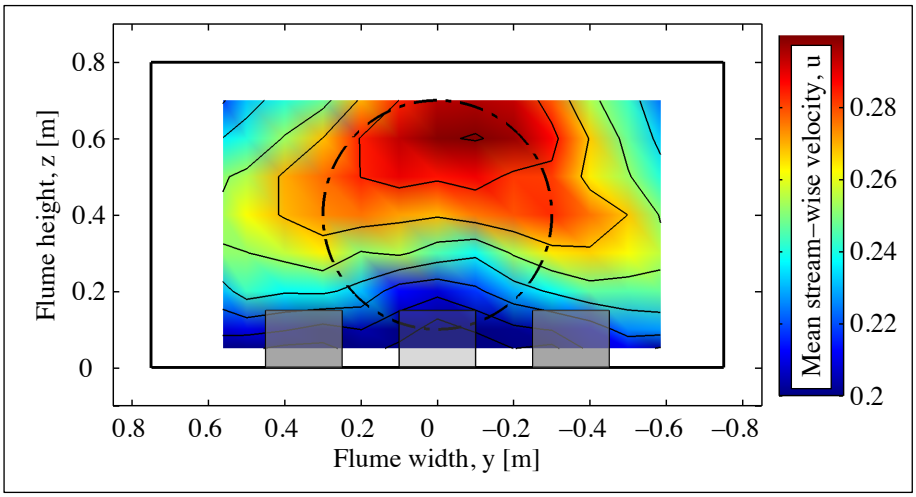

a. Mean stream-wise velocity, u [ms^{-1}].

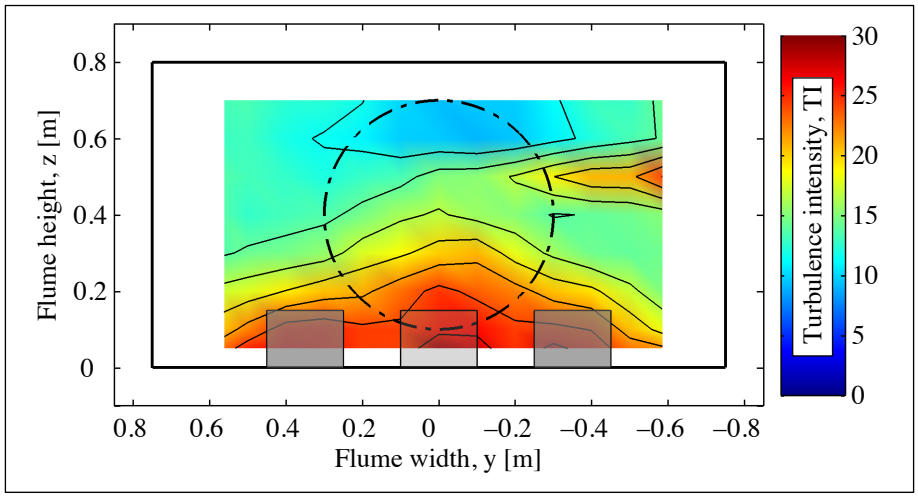

b. Turbulence intensity, TI [%].

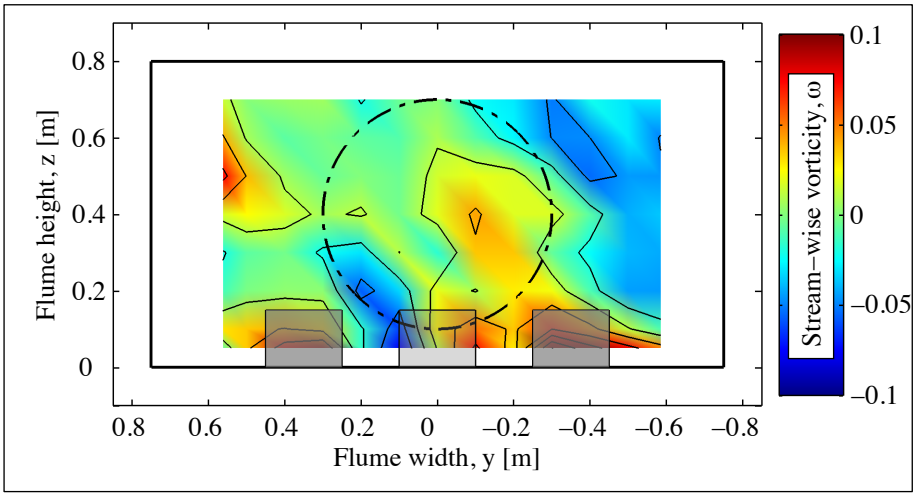

c. Stream-wise vorticity, ω_x [s^{-1}].

Figure 2.1.3: High turbulence intensity turbine plane measurement grid (*U0, T1*).

2.1.3 Calculation of Flume Wall Roughness Height

Regions of velocity shear reaching from each wall a considerable distance into the centre of the velocity grid, δ=0.6[m], are clearly visible in Figure 2.1.2a. A profile taken from the centerline of this velocity grid is reproduced in Figure 2.1.5 to further highlight the extent of this shear. Generated by the no-slip condition and grown along the full length of the EDF flume, the characterization of these velocity profiles (boundary layers) is an important first step towards representation of the flume environment within the numerical domain.

Within turbulent boundary layers the magnitude of shear stress σ_w close to the wall can be assumed constant with height, Duncan *et* al. (1970). We may form a velocity scale representative of this shear stress, termed the friction velocity u_f, according to

$$u_f = \left[\frac{\sigma_w}{\rho}\right]^{\frac{1}{2}}. \tag{2.4}$$

The rate of strain within turbulent boundary layers is shown by Plate (1971), via dimensional arguments, to be proportional to the ratio of friction velocity to height

$$\frac{\partial u}{\partial z} \propto \frac{u_f}{z}. \tag{2.5}$$

Assuming that momentum transport via turbulent eddies (characterized by an eddy viscosity μ_t) is far greater than that achieved by laminar shear ($\mu_t >> \mu$), σ_w can be shown to be proportional to the strain rate as follows

$$\sigma_w \propto \left(\mu_t + \mu\right)\frac{\partial u}{\partial z} \sim \mu_t \frac{\partial u}{\partial z}. \tag{2.6}$$

Combining and integrating Eqs. (2.5) and (2.6) provides an expression for the mean flow speed within the boundary layer as a function of wall normal distance normalized on a parameter known as the wall roughness height z_o

$$\bar{u}(z) = \frac{u_f}{\kappa} \ln \frac{z}{z_o}. \tag{2.7}$$

Defining friction velocity u_f (representative of the scale of the fluctuations) as

$$u_f = \frac{\kappa \bar{u}}{\ln \frac{z}{z_o}} \tag{2.8}$$

and incorporating Von Kármán's constant κ=0.4.

This 'law of the wall' scaling is found to be applicable to a large range of wall bounded flows. As such, many numerical codes, including FLUENT, incorporate 'wall functions' allowing the specification of wall roughness via a wall roughness parameter z_o.

The wall roughness parameter can be calculated from the experimental velocity profiles provided by EDF; enabling matching of the influence of wall roughness in the flume to that represented within the simulations. Solving Eqs. (2.7) and (2.8) iteratively provides a means for this roughness height estimation. Figure 2.1.5 illustrates the resulting fit between the law of the wall profile using a converged roughness height estimate $z_o = 3.21 \times 10^{-6}$m and the experimental data.

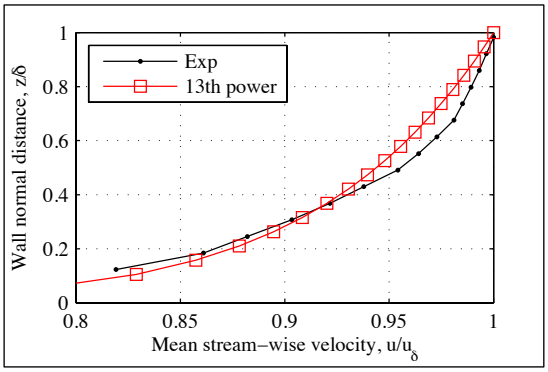

Figure 2.1.4: Illustration of an approximate 13th power law fit to flume data.

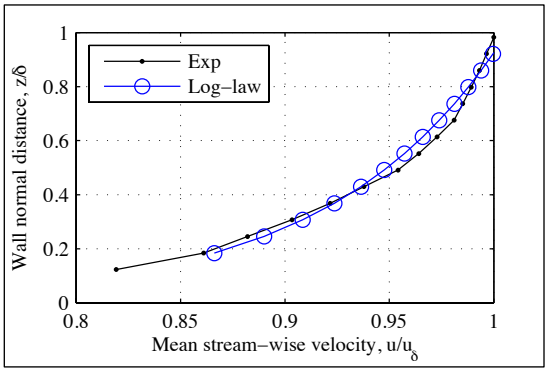

Figure 2.1.5: Illustration of log-law fit with velocity profile data measured by EDF.

In addition to providing a robust estimate for wall roughness, knowledge of the velocity profile enables an improved specification of the volumetric flow rate

within the simulations. This is achieved via the specification of a velocity profile at the inlet boundary condition as opposed to a uniform velocity profile. As the modelling of the outer flow is also important in this case a power law profile (Figure 2.1.4) is chosen in preference to the log-law fit as it better represents the region $z>\delta$. The development of numerical models of the flume environment and verification of these techniques is further discussed in Section 2.2.

2.1.4 Calculation of Turbulence Length Scale

A temporal autocorrelation function is applied to a time-series of velocity data to calculate the turbulent length scales presented in Figure 2.1.6, Mathieu & Scott (2000). The velocity, $u(t)$, at time t is correlated with that at time τ later, $u(t+\tau)$, to form a velocity correlation, $R(\tau)$, or the velocity correlation coefficient, $\rho(\tau)$:

$$R(\tau) = \overline{u(t)u(t+\tau)}; \tag{2.9}$$

$$\rho(\tau) = \frac{R(\tau)}{\overline{u^2}}; \tag{2.10}$$

where the over-bar indicates a time mean over a period far longer than that of the turbulent fluctuations. Integrating the correlation coefficient over all interval separations τ, develops the correlation time scale Θ, and from this the time mean bulk velocity, U, the turbulence length scale, L, may be found.

$$\Theta = \int_{-\infty}^{\infty} \rho(\tau) d\tau \tag{2.11}$$

$$L = U\Theta \tag{2.12}$$

Applying the above procedure to the time signals provided by EDF for the *U0, T0* case yields the length scale variation indicated in Figure 2.1.6.

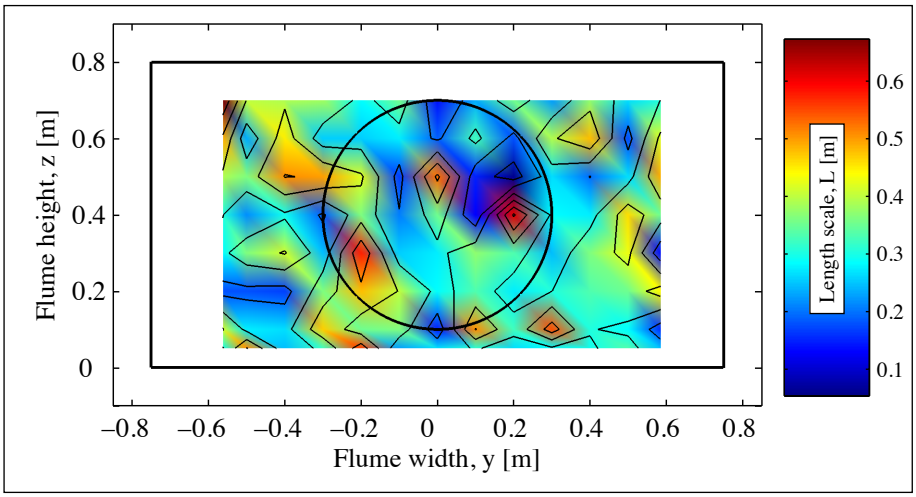

Figure 2.1.6: Contours of turbulent length scale across the rotor plane for flume test at - flow conditions *U0* and *T0*.

From the above analysis we determine a baseline length scale of L = 0.2m for the flow conditions *U0, T0,* to be used in all subsequent calculations to model the dissipation of turbulent kinetic energy.

2.1.5 Summary of the Flume Environment

A healthy and well-characterized flow environment is shown for the low turbulence intensity case *T0*. Flow uniformity across the turbine plane lends itself well to both experimental and numerical investigation and is considered representative of a low shear tidal environment. Moving to the high turbulence intensity *T1* case highlights far greater flow non-uniformity across the rotor plane. The presence of strong and persistent stream-wise vorticity shed from breezeblock roughness elements is postulated to be the cause.

The centreline dip in mean velocity and associated increase in turbulence intensity occurring across the lower third of the rotor plane is not considered representative of typical tidal flows and is thus an undesirable characteristic of the present *T1* environment.

It was suggested that alignment of the breezeblocks perpendicular to the flow, in strips occupying the full span-wise width of the flume, could improve the flow environment for the *T1* case. Here, flow separation over each roughness element would be constrained to take a much more two-dimensional form; limiting the

extent of stream-wise vorticity introduced into the flume whilst still promoting mixing in a vertical sense.

This perpendicular breezeblock case has subsequently been tested by EDF along with a number of other configurations in an effort to remove the velocity dip from the high velocity, high roughness case. Unfortunately, the dip has persisted for all configurations tested. EDF identify Prandtl's secondary flow instability of the second kind as the primary mechanism responsible for the centerline velocity dip, Tamburrino *et al* (1999), Nezu *et al* (2005). The University of Oxford suggested that a wider velocity measurement grid extending from wall to wall could be used to better visualize the flow along the flume's corners and perhaps verify this hypothesis.

Figure 2.1.7 illustrates this widened base-line flow map showing cross-stream velocity vectors for the low speed high turbulence intensity test case (*U0, T1*). The presence of persistent stream-wise structures is clearly visible in this time-averaged flow-field. Salient flow features comprise: roughly symmetrical

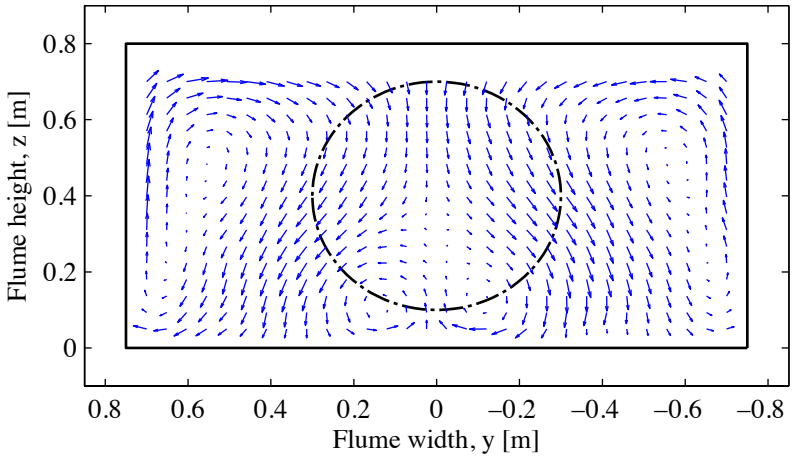

Figure 2.1.7: Cross-stream velocity vector map highlighting Prantl's secondary flow instability of the second kind for open channel flume test at flow conditions *U0* and *T1*.

structure in the vertical plane; centerline upwelling at the floor, injecting low momentum fluid upwards resulting in the previously observed centerline velocity dip; centerline down-welling at the free surface, drawing high momentum fluid lower in the vertically sheared profile; mean flow directed towards the flume corners, recirculating both back along the floor towards the

flume center and up along the side-walls towards the free surface. The magnitude of these time averaged cross-stream velocity components is observed to be on the order of 2% of the mean stream-wise flow velocity, resulting in an overturn time of approximately 60-120 seconds.

Prandtl's secondary flow instability of the second kind is show by Nezu *et al* (2005) to be generated by turbulent anisotropy driven by interleaved velocity shear profiles extending from the flume walls and floor. The instability manifests in corner-driven vortices that meander across the plane orthogonal to the stream as they convect downstream. The centerline velocity deficit seen in the time-mean statistics is in fact the consequence of the temporal averaging of these corner-driven meandering vortices with an otherwise time-invariant hill-shaped flow profile (characterized by the intersection of orthogonal boundary layers emanating from both flume base and side walls).

Physically tidal turbines may encounter such large-scale flow structures with axes aligned both with and orthogonal to the tidal stream. Hence, both *T0* (low intensity, clean flow) and *T1* (high intensity, complex flow with large coherent structures) present useful experimental test cases for understanding turbine performance and wake structure. However, it should be noted that it is unlikely that a real turbine's time-mean profile would ever present a centerline velocity deficit – this is not however considered to be materially significant.

To correctly simulate the flume corner-driven vortex structures and their influence on the model rotor and its wake, one should simulate the time-invariant hill profile with added time resolved synthetic eddy structures at inflow to represent the corner-driven vortices. Further, it may also be necessary to use an anisotropic turbulence model representative of the flow environment so as not to artificially dissipate the synthetically imposed structures. Such an approach lies beyond the scope of the current flume-scale investigation.

Within the present flume-scale investigation the *T1* environment will be modelled through simulation of the time-invariant hill profile without the presence of corner-vortices. The impact of these vortices is unknown and cannot be determined *a priori*. However, we speculate that such eddies may influence the turbine through both vortex-blade impingement events as well as through

enhanced wake mixing. Whilst the former cannot be properly treated without the modelling of synthetic eddies, the effects of the latter may be representable through adjustments to the turbulence model. Depending on the results of numerical-experimental comparisons, such adjustments may be pursued if believed necessary and worthwhile from the point of view of modelling full-scale turbines in real tidal flows.

2.2 Bare Flume Simulations

Numerical modelling is carried out on the flume in isolation in order to ensure satisfactory reproduction of the flow physics. Understanding gained from component-level testing of the flume model is subsequently utilized in the full turbine simulations presented in Section 4. At all times we seek to minimize computational expense whilst preserving an accurate simulation of the pertinent flow physics.

During model development, various sub-tasks are undertaken. Firstly, the rate of growth of a turbulent boundary layer on a two-dimensional flat plate is calculated numerically and compared with experimental data. Next, a study is carried out on the influence of wall roughness and inflow turbulence upon the boundary layer. Turbulence intensity and length scale profiles are calculated numerically and compared to data derived from EDF's experiments. Finally, to minimise computational expense, the upstream region is reduced in length and a fully developed velocity profile is applied as an inlet boundary condition. Calculations have been conducted using a rigid lid as well as a free-surface model for both 2D and 3D flume geometries (Section 2.3).

It is important to note here that a single turbulence model must be used throughout the computational domain. Whilst flume simulations are carried out using both the k-ω SST and k-kl-ω turbulence models, component level blade testing primarily drives the choice of turbulence model (k-ω SST). In the interests of brevity, results are presented only for the k-ω SST turbulence model.

2.2.1 Boundary Layer Growth Along a Two-Dimensional Flat Plate

There are two methods of modelling a boundary layer within FLUENT when using the k-ω SST turbulence model. The first method is to resolve the boundary layer fully, by ensuring sufficient grid resolution in the wall-normal direction to capture the viscous sublayer. Sufficient resolution is obtained for a non-dimensional wall-adjacent cell height, $y^+ \sim 1$

$$y^+ = \frac{u_f y}{\nu}, \tag{2.13}$$

where y is the normal distance from the wall. The second method available in FLUENT, for or wall-adjacent cell heights with $y^+ > 60$, is to apply a wall function based on the law-of-the-wall for a turbulent boundary layer. Use of this model enables the flow field to be modelled accurately across a relatively large wall-

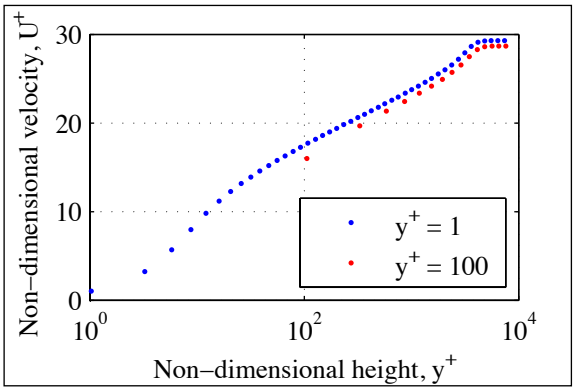

Figure 2.2.1: An illustration of a turbulent boundary layer profile resolved with and without the use of wall functions.

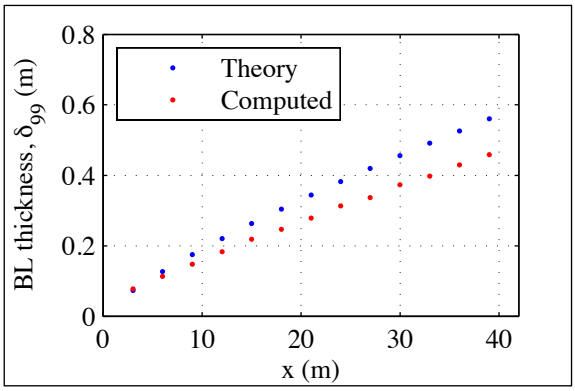

Figure 2.2.2: An illustration of boundary layer growth along a flat plate. Comparison of theory with computation.

adjacent cell, leading to considerable savings in computational effort.

Close to the rotor plane a favorable pressure gradient exists, inferring that boundary layer separation should not occur, hence permitting the use of wall functions. Figure 2.2.1 compares profiles for a fully resolved ($y^+ = 1$) and wall function modelled ($y^+ = 100$) boundary layer. A good agreement is achieved between the two methods.

Figure 2.2.2 compares the simulation of turbulent boundary layer growth, here represented by the 99% boundary layer height δ^{99}, along a zero pressure

gradient flat plate with the analytic expression assuming a $\frac{1}{7}$ power law velocity profile, Massey (1989),

$$\delta^{99} = 0.3707x\left(\frac{\nu}{U_\infty x}\right)^{\frac{1}{5}}, \qquad \textbf{(2.14)}$$

where U_∞ is the free stream velocity and x is the stream-wise distance along the flat plate. A stream-wise pressure gradient formed along the computational domain is the likely cause of the small disparity present in Figure 2.2.2. Aside from this, the general trend of the developing boundary layer is captured well.

2.2.2 Influence of Wall Roughness Height and Inflow Turbulence

Two mechanisms are employed to generate the desired turbulence intensity profile in the computational model: turbulence intensity and length scale are specified at the inflow boundary; and wall roughness parameters are set to ensure generation of turbulent kinetic energy within the boundary layer as the flow progresses along the flume. A full explanation of the wall roughness parameters is given in Section 2.1.3. The general effect of inflow turbulence and wall roughness is presented in Figure 2.2.3 for the case of a two-dimensional model of the flume. Two roughness heights are specified; smooth corresponds to a roughness height of 0m, whilst rough corresponds to a roughness height of 0.01m. Note that for this particular investigation the choice of roughness height was arbitrary. The roughness parameters for the final model are retrieved from experimental data, as explained in Section 2.1.3. Two inflow turbulence intensities, 1% and 5%, are considered.

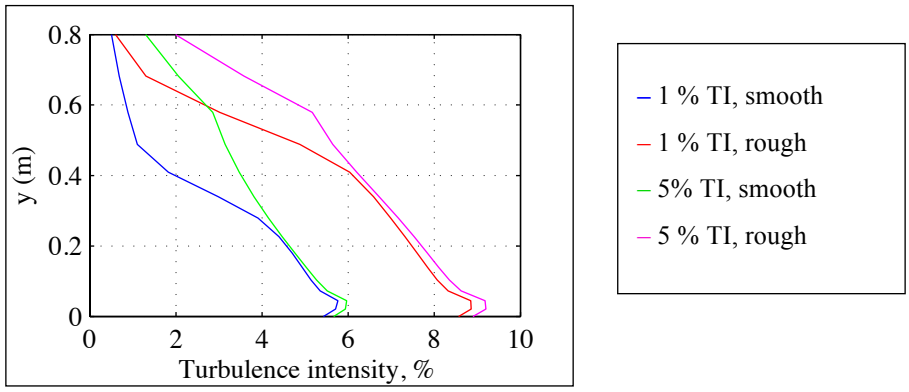

Figure 2.2.3: Effect of inflow turbulence and roughness height on turbulence profile. Profiles taken at a downstream distance of 36 meters (corresponding to the position of the rotor plane). The free-surface is modelled as a rigid lid.

A number of conclusions are drawn from the results of this study:

I. wall roughness and inflow turbulence intensity can be used to control the turbulence intensity at a given station in the flow, however;
II. turbulence intensity prescribed at the inlet boundary dissipates rapidly as the flow progresses;
III. the influence of wall roughness on turbulence intensity reduces with distance from the boundary;
IV. a considerable distance is required to allow the turbulence profile to develop;
V. turbulence intensity is dampened by the rigid-lid boundary condition at the surface of the fluid.
VI. together, the ability to specify both wall roughness and levels of inflow turbulence enables the recreation of a turbulent environment close to that observed in the experimental flume. However, as previously noted in Section 2.1.5, the use of an isotropic turbulence model prevents the simulation of the flume instability and associated stream-wise vorticity / mixing.

2.2.3 Turbulence Intensity Profile

Planar profiles of turbulence intensity from the numerical model are compared with experimental data from the flume. For this comparison, a three-dimensional computational model is created, based on the dimensions of the

experimental flume (Section 3.1.3), with the rotor plane placed 36.8m downstream of the inlet. The sectional width and height are 1.5m and 0.8m respectively. A slip surface boundary condition is used to approximate the free surface. A turbulence intensity of 5% and a turbulence length scale of 0.1m* are prescribed at the inlet. The wall roughness height, as calculated from experimental data at flow conditions *U0* and *T0* in Section 2.1.3 is set to z_o=3.21×10^{-6} m.

* A heuristic choice of 0.1m is made to inform initial calculations. Subsequent length scale analyses, such as that given in Figure 2.1.1, are used to improve this estimate.

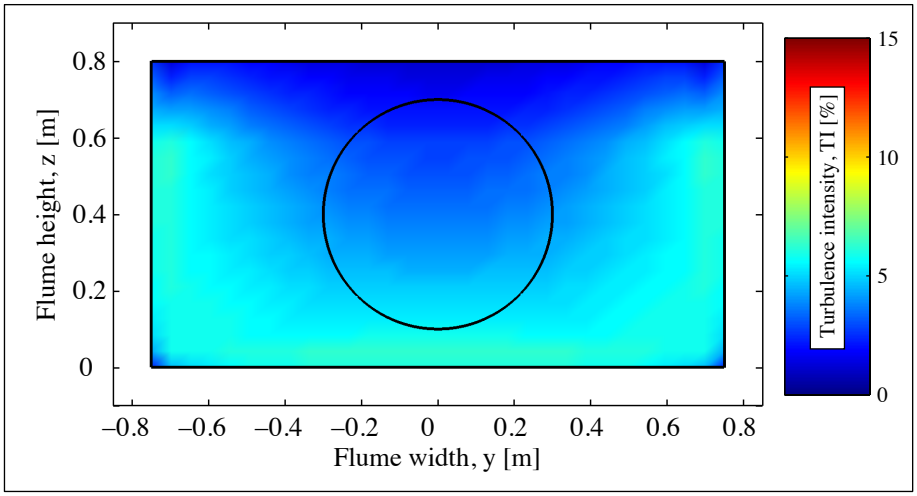

(a) Computation.

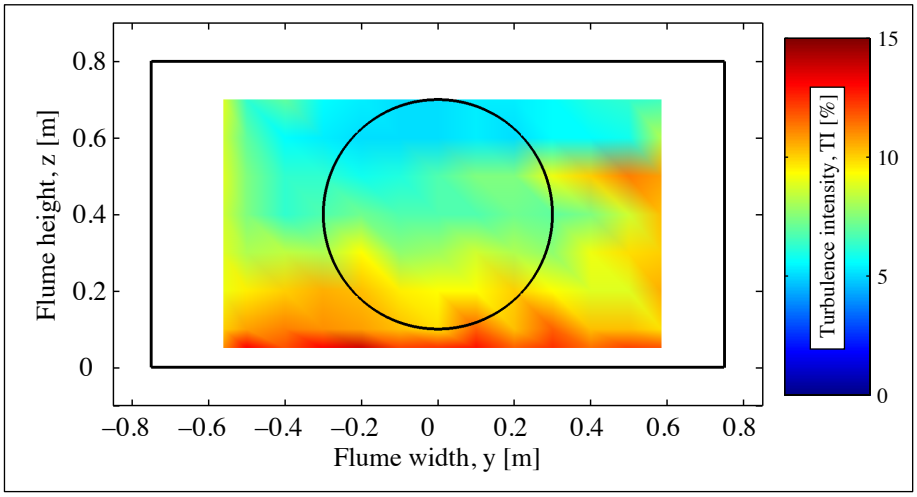

(b) Experiment.

Figure 2.2.4: Illustrations of the turbulence intensity profile across the rotor plane (x=36.8 m).

Figure 2.2.4 compares experimental turbulence intensities with computation. Whilst similarities exist, for the inflow conditions trialed, the numerical result is shown to lie an order of magnitude below the experimental profile. Increased levels of background turbulence intensity specified at the model inflow, simulating promoted mixing resulting from the secondary flow structures discussed in Section 2.1.5, is found to be short lived. The absence of these secondary flow structures within the isotropic numerical model, artificial dissipation and an ill-posed inflow condition are considered responsible for the premature decay of turbulence intensity in the stream-wise direction.

Details of steps taken to match the turbulence conditions at the rotor plane more closely to those provided by experiment are a subject of ongoing work by the University of Oxford. As previously stated, whilst it may be possible to use an anisotropic turbulence model representative of the flow environment so as not to artificially dissipate the synthetically imposed structures. Such an approach lies beyond the scope of the current flume-scale investigation.

2.2.4 Velocity Profile

Significant savings in computational effort are made via a reduction in the upstream length of the flume model. This is achieved by matching developed velocity and turbulence profiles at the inlet of the reduced length numerical domain to experimental observations.

The present flume simulations are created with an inflow boundary set three rotor diameters upstream of the rotor plane. An algebraic inlet velocity profile based on a $\frac{1}{13}$ power law, is used. The selection of this power law results from a data fit with the experimental flume test data presented in Section 2.1.3. Figure 2.2.5a illustrates the application of an inflow velocity profile constructed from a combination of three power-law functions simulating boundary layer growth from each of the flume walls as well as the floor. Figure 2.2.5b presents the corresponding velocity field extracted at the rotor plane showing the maintenance of the desired inflow velocity profile within the flume right up to the rotor plane.

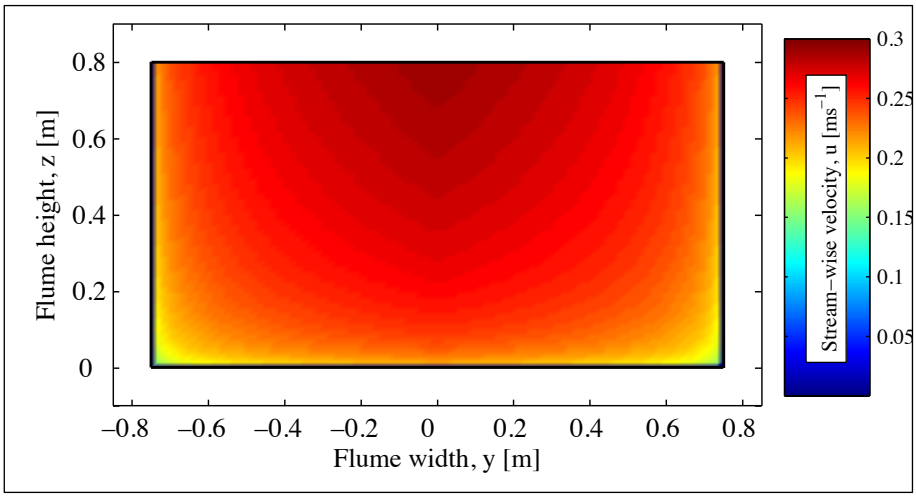

(a) Inlet boundary.

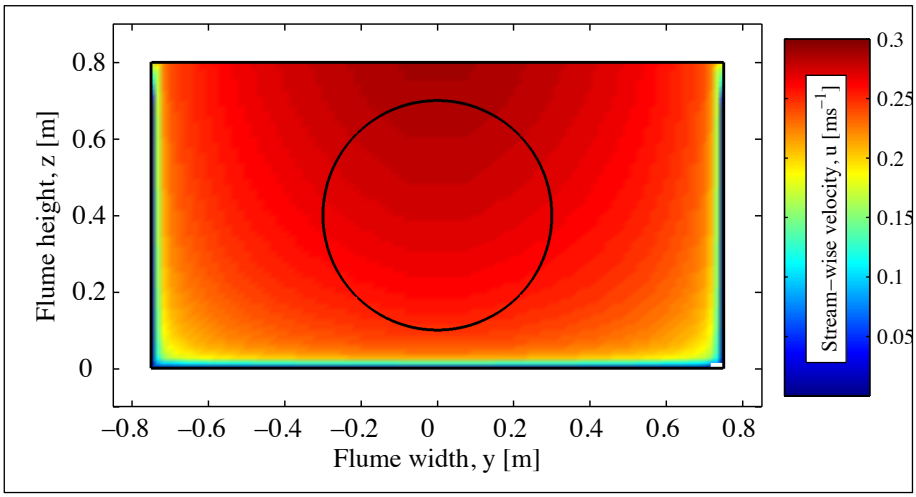

(b) Rotor plane.

Figure 2.2.5: An illustrative example of an inflow velocity profile, constructed from a combination of three power-law functions, showing maintenance of the desired profile right up to the rotor plane.

Work is currently being carried out to match profiles of turbulence intensity and length scale at the inlet boundary of the numerical model with profiles from the EDF flume.

2.3 Free-surface Capture

The influence of free surface proximity on the operation of tidal turbines in both flume scale tests and the full-scale tidal environment is not yet fully understood. Whilst significant contributions have been made to the

understanding of tidal energy extraction in highly blocked two-dimensional open channel flows (Whelan *et al.* 2009, Houlsby *et al.* 2008) a full understanding of the three-dimensional environment is still under development. As such work is underway to develop techniques capable of modelling such three-dimensional energy extraction, including localized effects due to momentum extraction by the turbine.

2.3.1 Volume of Fluid

A Volume of Fluid (VOF) method is employed within FLUENT to capture the instantaneous position of the free surface. The air-water interface is tracked via the solution of an additional set of momentum equations

$$\frac{1}{\rho_q}\left[\frac{\partial}{\partial t}\left(\alpha_q \rho_q\right) + \nabla \cdot \left(\alpha_q \rho_q \vec{v}_q\right) = \sum_{p=1}^{n}\left(\dot{m}_{pq} - \dot{m}_{qp}\right)\right] q = 1 \ldots n\,, \qquad \textbf{(2.15)}$$

which govern the evolution of the volumetric fractions α_q of the *n* phases present in each cell

$$\sum_{q=1}^{n} \alpha_q = 1\,. \qquad \textbf{(2.16)}$$

The rate of mass flow from cell *p* to *q* and *q* to *p* are defined as $\dot{m}_{pq}$ and $\dot{m}_{qp}$ respectively.

Fluid properties (density and viscosity) for cells containing an air-water mix (spray) close to the free surface are calculated via a linear interpolation with respect to volume fraction for each constituent phase.

2.3.2 Analytical Test Case

A simple test case with an analytical solution Duncan (1970) is employed in order to verify the free surface technique discussed in Section 2.3.1. Here, a two-dimensional channel comprising a gently sloping forward facing bed ramp (Figure 2.3.1) is chosen to simulate the effect of energy transfer on free surface elevation.

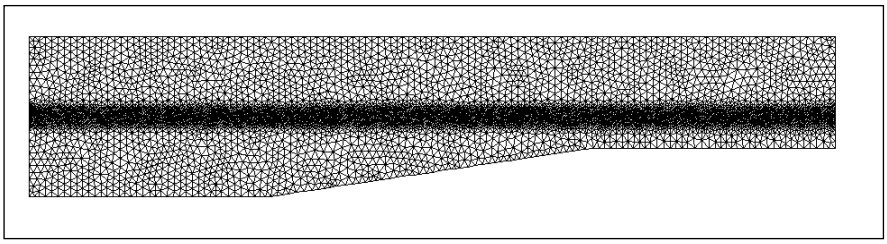

Figure 2.3.1: An Illustrative example of the forward facing bed ramp test case showing an increased mesh resolution ether side of the free surface interface zone (h/h_1=0.6).

By imposing a change in the channel bed height an energy transfer from hydraulic head (sum of pressure and gravitational potential) to kinetic takes place; akin to the bulk energy transfer between hydraulic and kinetic head observed for tidal flow turbines. The selection of the bed ramp test case enables a direct comparison to theory to be made.

If the bed slope is gentle then we may assume that energy is conserved such that for a bed ramp of height h

$$h_1 + \frac{v_1^2}{2g} = h + h_2 + \frac{v_2^2}{2g}, \qquad \textbf{(2.17)}$$

where h_1, v_1 and h_2, v_2 are the water depth and flow velocity upstream and downstream of the ramp. The reduction in free surface elevation, x, is therefore

$$x = h + h_2 - h_1. \qquad \textbf{(2.18)}$$

Assuming uniform flow at both inlet and outlet, Eqs. (2.17) and (2.18) can be combined with a statement of mass conservation

$$v_1 h_1 = v_2 h_2, \qquad \textbf{(2.19)}$$

to give free surface height change *x* as a cubic in terms of inlet Froude number

$$Fr_1 = \frac{v_1}{\sqrt{gh_1}}, \qquad \textbf{(2.20)}$$

and the ratio of the height of the bed ramp to the inlet flow height h/h_1

$$\frac{x^3}{h_1} + 2x^2\left(1 - \frac{h}{h_1} - \frac{Fr_1^2}{4}\right) + x\left(h_1 - h\right)\left(1 - \frac{h}{h_1} - Fr_1^2\right) + \frac{Fr_1^2}{2}h\left(2h - h_1\right) = 0. \qquad \textbf{(2.21)}$$

Solving Eq. (2.21) for conditions representative of tidal flows, subcritical at both inlet and outlet, provides an analytical framework for the free surface model validation.

2.3.3 Implementation of VOF model

The simulation of flows via the numerical integration of the Navier-Stokes equations requires the specification of boundary conditions along all domain boundaries. Typical boundary conditions for the solution of open channel flows involve the specification of a free surface height and velocity at the inlet, non-slip / non-penetration walls and a static pressure distribution at the outlet. When a variation in density is present between two immiscible phases, as is the case for the air / water interface under study, gravitational forces become significant and a static pressure distribution including the variation of hydrostatic pressure with depth below the water surface is required for subcritical outlet flows. As such, outlet water height becomes an additional problem constraint.

The specification of water depth at the outlet causes significant problems to the solution of any free surface problem involving energy extraction or exchange within the domain. By fixing the outlet height the problem becomes fully constrained resulting in non-physical discontinuities (waves corresponding to erroneous energy sources and sinks), typically found at the inlet, to occur when the net energy exchange within the domain is not reflected by the relative water depths at inlet and outlet. For subcritical flows a net energy extraction results in a decrease in water depth across the domain and vice versa.

As the level of energy extraction / performance of a tidal turbine is not known *a priori*, an iterative technique is required to solve for outlet height; balancing energy extraction within the domain to that reflected along the solution boundaries. This is accomplished via the use of a User Defined Function (UDF) written and implemented within the FLUENT environment. This function, evaluated at each time step, sets the outlet water depth, h_{out}, using a simple proportional feedback loop that recursively adjusts h_{out} to achieve the desired inflow condition, h_{in}, without the perturbations in free surface elevation that characterize energy-incompatible inflow-outflow conditions: (the logic of the loop below starts by assuming that h_{out} is too high resulting in an unphysical surface height h_{us} shortly downstream of the inflow boundary)

i. upstream water depth h_{us} evaluated a short distance (~$2h_{in}$) downstream of the inlet via a linear interpolation between phases;
ii. upstream depth compared to target inlet height h_{in} to calculate a height error $h_{err} = h_{in} - h_{us}$;

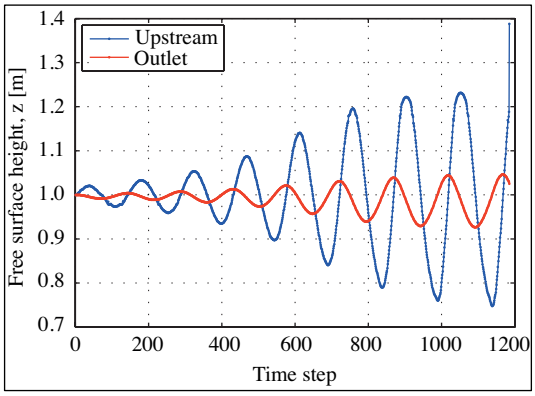

Figure 2.3.2: High *k* Free surface oscillations (h_{us} – blue, h_{out} – red).

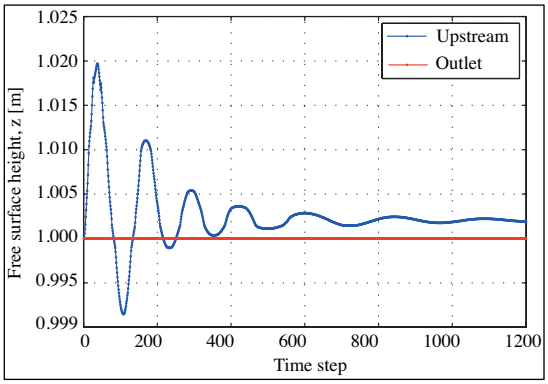

Figure 2.3.3: Low *k* Free surface oscillations (h_{us} – blue, h_{out} – red).

iii. height error multiplied by a gain k and the current time step size, Δt, and used to set a new outlet height $h_{out} = h_{out\_old} - k\Delta t\, h_{err}$.

As the solution is stepped forward in time, over-predictions in energy extraction within the domain, i.e. h_{out} too small, result in h_{us} falling below the target inlet height and vise versa. Tuning the feedback loop via adjustments in k enables a fast acquisition of the target height with limited overshoot. Illustrative examples of the influence of k are shown in Figure 2.3.2 for a high gain case, resulting in

solution instability, and in Figure 2.3.3 for a stable solution using a reduced feedback gain.

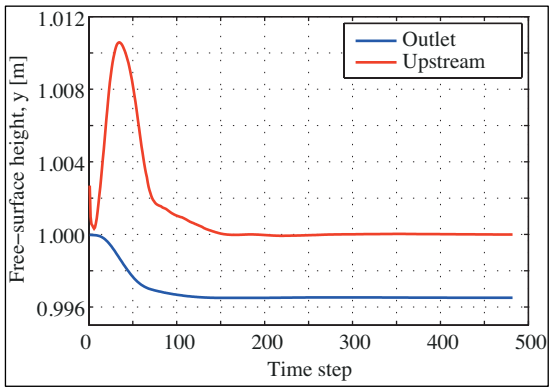

Figure 2.3.4: Illustration of free surface convergence employing inlet damping.

It is found that solution convergence can be increased via a complementary transient adjustment to the inflow velocity boundary condition and hence volumetric flow rate at the inlet. By reducing volumetric flow below target when h_{us} is found to lie above h_{in}, and vice versa, the free surface oscillations seen in Figure 2.3.2 and Figure 2.3.3 can be greatly damped. The transitory adjustment to the inlet velocity u_{in} is calculated as flows

$$u_{in} = u_1\left(1 + D\frac{h_{err}}{h_{in}}\right), \qquad \textbf{(2.22)}$$

where u_1 is the target inlet velocity and D is a damping parameter controlling the inlet adjustment. As h_{err} falls to zero it is clear from Eq. (2.22) that the original target inlet velocity will be recovered. In order to reduce high frequency noise (waves) entering the domain via Eq. (2.22), u_{in} is passed through a Butterworth second order low pass filter prior to application to the inlet boundary condition. An illustrative example of the effectiveness of inflow damping in reducing times to convergence is given in Figure 2.4.4; displaying a converged outlet height within 200 time-steps, a substantial improvement to the ~1200 time-steps required for the undamped case (Figure 2.3.3).

2.3.4 Validation of VOF model

A number of two-dimensional open-channel flow simulations using FLUENT combined with the UDF discussed above are now performed in order to validate the developed method with theory for the case of the gradual forward facing bed ramp described by Eq. (2.21). Figure 2.3.5 presents a matrix of comparisons, representative of typical tidal turbine scenarios; varying ramp

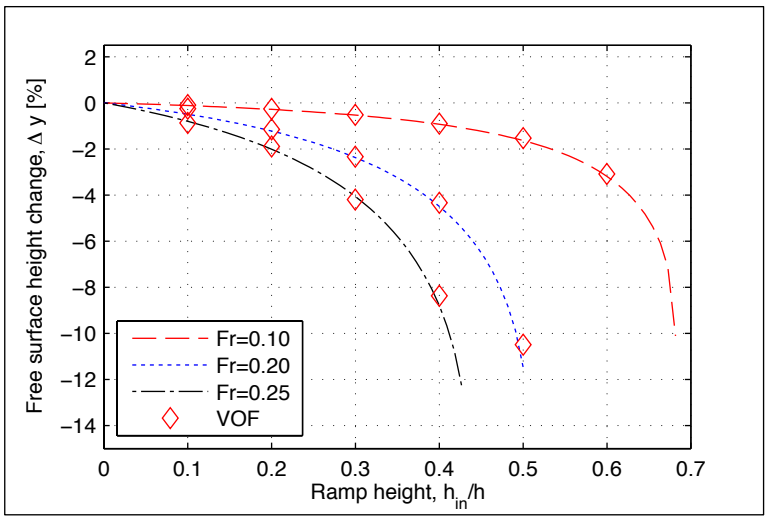

Figure 2.3.5: Free surface height change, $\Delta y=1-(h_{in}/h_{out})$, for flow over a forward facing bed ramp; computations and theory.

height from 10% to 60% of inlet depth in 10% increments over three inlet Froude numbers; Fr_1 = 0.1, 0.2 and 0.25. Calculations for various step heights are performed on a set of grids topologically similar to that shown in Figure 2.3.1. Agreement between the present model and theory is shown to be excellent over the range of Froude numbers and ramp height ratios considered, successfully validating the developed technique.

3 Rotor Model Verification

Extremely large grids, often on the order of millions of cells, are found necessary for the successful simulation of three-dimensional turbine flows (Ferrer 2007). The shear scale of these computations and three-dimensional nature of the stencil renders any form of formal grid convergence study using uniform refinement unrealistic considering available time scale and computational resource.

Considering the above factor of problem scale, rotor model verification is performed on a component-by-component basis for the two most fluid-dynamically significant components. The rotor blades, presented in Section 3.2, and the rotor tower, presented in Section 3.3. Component validation is achieved via comparison with experimental data wherever possible.

Prior to these component-by-component studies, a description of the full rotor geometry illustrating the relative locations of each component and their proximity to the tunnel walls is briefly presented in Section 3.1.

3.1 Geometry Generation

With the exception of the rotor blades, provided by GL Garrad Hassan to the University of Oxford as CAD readable files, all additional geometric components have been generated in-house from a number of dimensioned drawings. As such, brief descriptions of the methods used to generate the required CAD files for each constituent part, including any alterations made, are detailed below.

3.1.1 Rotor Blade Geometry

GL Garrad Hassan has provided a description of the rotor blade, designed by TGL as part of deliverable WG4 WP1 D1, in the form of a CAD readable file.

Two minor alterations are required to enable a three-dimensional mesh to be generated around the CAD blade geometry file. The first alteration involves patching a pin-hole on the surface of the blade tip. Secondly, the blade root is extended by 5 mm to ensure a good-quality interface with the hub geometry.

3.1.2 Turbine Assembly Geometry

The majority of the dimensions required to fully define the tower, nacelle and hub components are retrieved from engineering drawings provided to the University of Oxford by Jeremy King. Additional dimensions absent from the drawing, for example locations of shoulder features and the profile of the hub, were extracted using an image analysis application to probe an electronic copy of the drawing for the required information.

In the interest of the efficient use of computational resources during development of the three-dimensional numerical model, minor features of the original geometry are simplified or omitted outright. Such features, considered to be fluid-dynamically insignificant, include flanges, fasteners, and keyways.

The diameter of the tower has been scaled down by a factor of 70% with respect to the actual dimension in order to model its effect on the flow field appropriately. Justification for this action is given in Section 3.3.4. Figure 3.1.1 provides an illustrative isometric projection of the complete rotor assembly modelled in Section 4.

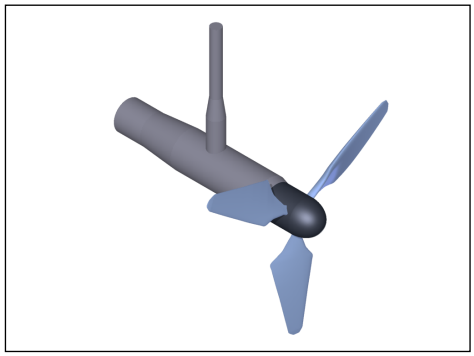

Figure 3.1.1: Isometric view of turbine as modelled from engineering drawings provided by Jeremy King.

3.1.3 Flume Geometry

Figure 3.1.2 and Figure 3.1.3 illustrate the sectional and stream-wise dimensions of the experimental facility provided to the University of Oxford by EDF.

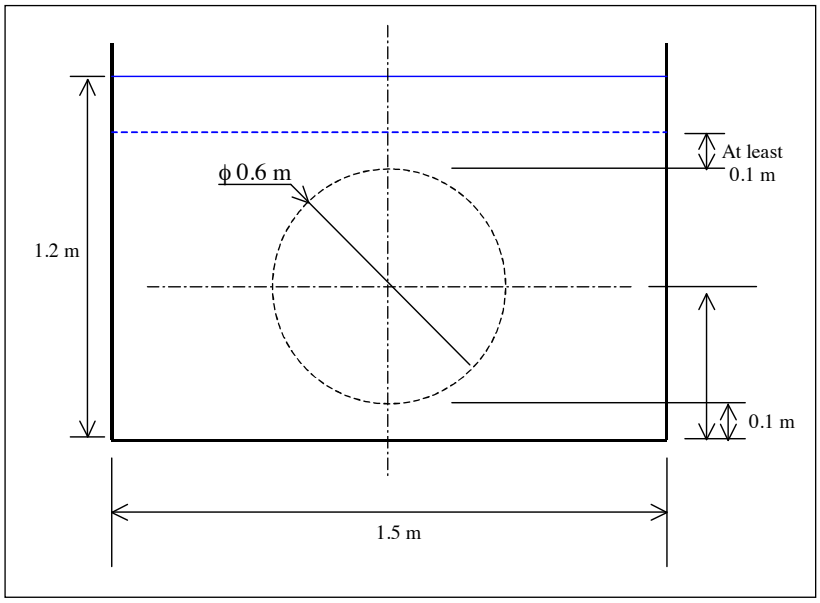

Figure 3.1.2: Sectional dimensions taken from document WG4WP1D1.

Within the flume, the upstream region is assumed to start at the end of the final flow-straightening grid x = 57m and end at the rotor plane x = 20.20m (Figure 3.1.3). This results in a total upstream length of 36.8m, which has been used for

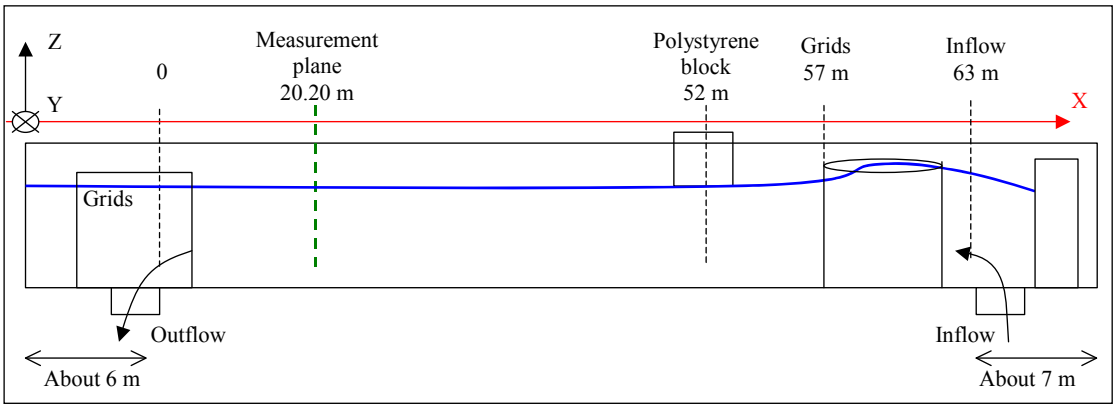

Figure 3.1.3: Stream-wise dimensions taken from document WG4WP1D3.

numerical investigations into wall roughness and inflow turbulence parameters (Section 2.2.3). By specifying velocity and turbulence profiles for fully developed flow, this upstream length can be greatly reduced. The upstream distance was set at three rotor diameters for the full three-dimensional simulations described in Section 4.

3.2 Rotor Blade Component Verification

A reduction in problem scale from the full rotor assembly to an individual aerofoil section enables both verification of the rotor blade mesh via a grid independence study and comparison to wind tunnel data on a component basis.

3.2.1 Blade Element Analysis of the Flume Scale Rotor

Prior to commencing a blade component validation exercise, a blade element model BEM is constructed to better understand the interplay between constant chord aerofoil performance and its influence on integral rotor performance metrics such as power coefficient C_p and thrust coefficient C_x. Whilst not applicable to all problems, BEM models form an incredibly cheep, fast and surprisingly accurate toolset for the prediction of turbine performance in unconstrained flows.

Documentation detailing the construction of blade element models applied to horizontal axis flow turbines readily available in the literature, Freris (1990). As such, rigorous descriptions of the techniques used are omitted in favour of a broad overview.

The present BEM model comprises multiple stream-tubes dividing the flow through the rotor into ~50 concentric annuli. Experimental aerofoil data taken from Miley (1982) for a NACA 4415 aerofoil is employed to model blade loads in the attached flow regime. For angles of attack exceeding stall, a post stall model by Viterna & Corrigan is employed, Viterna (1981). Induced drag effects are accounted for using Prandtl's tip loss correction, Prandtl (1934).

In order to remain consistent with work conducted by Garrad Hassan using their own in-house BEM code, GHBladed, Whelan (2010) approximate blade data for a Reynolds number Re=121,500 is employed; taking the mean of the Re=83,000 and Re=160,000 data sets tabulated in Miley (1982).

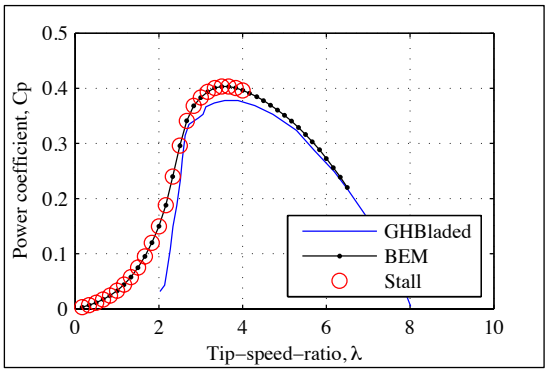

Figure 3.2.1: C_p prediction comparison between present BEM model and GHBladed.

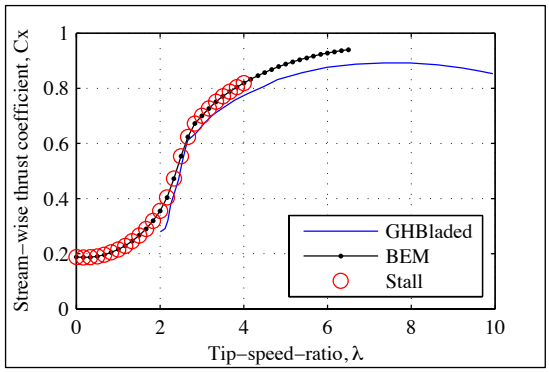

Figure 3.2.2: C_x prediction comparison between present BEM model and GHBladed.

Figure 3.2.1 and Figure 3.2.2 illustrate a good comparison between the present BEM technique and the well-developed industry standard wind turbine performance prediction tool GHBladed. Disparities are present at lower tip-speed-ratios where blade stall is indicated. This is considered due to differences in the implementation of the post-stall model. Accurate performance prediction within this rejoin ($\lambda < 2$) is however not considered necessary within the context of the present work. Both models predict maximum turbine performance at a tip-speed-ratio of $\lambda \sim 3.5$.

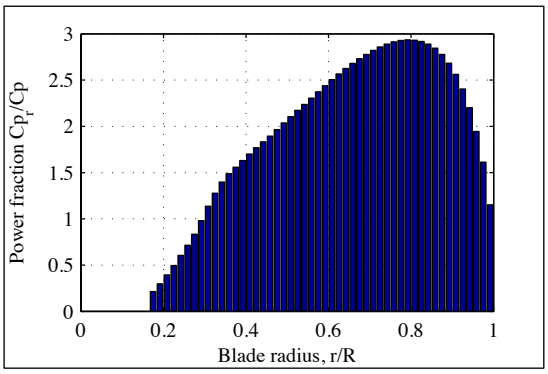

Figure 3.2.3: Fractional power production as a function of radial station ($\lambda = 3.5$).

Figure 3.2.3 illustrates the distribution of fractional power production as a function of radial station. A peak is shown to occur at 80% radius dropping at higher radii due to increased tip loss effects and at lower radii due to a reduction in local blade velocity with respect to the free stream.

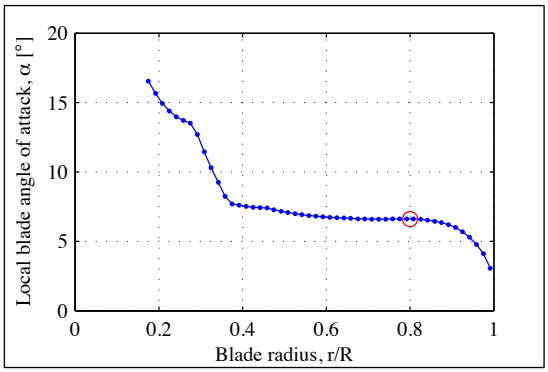

Figure 3.2.4: Blade angle of attack as a function of radial station for rotor operation at max Cp (λ = 3.5).

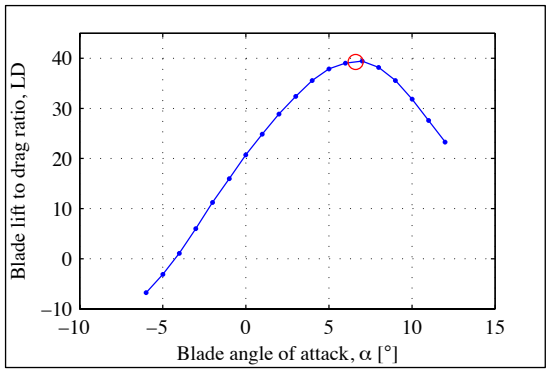

Figure 3.2.5: Lift to drag ratio calculated from experimental data highlighting blade angle of attack at 80% span extracted from rotor operation at max Cp (λ = 3.5).

Figure 3.2.4 shows local blade angle-of-attack as a function of radial station for a rotor operating at a tip-speed-ratio corresponding to a peak turbine performance (λ~3.5). Here, angle-of-attack can be seen to remain broadly constant α=6.6° across a large portion of the blade's radius. An illustration of aerofoil lift to drag taken from the experimental data-set Miley (1982) is presented in Figure 3.2.5. Here, the strong influence between this aerofoil performance metric and turbine performance is clear.

3.2.2 Summary of Blade Element Model Findings

Pertinent points arising from the blade element analysis of the flume scale rotor operating within an unbounded flow are as follows:

I. A maximum power coefficient of C_p~0.4 is attained a tip-speed-ratio of λ~3.5;
II. a large proportion of the rotor's total power output is generated at and around the 80% radial station;
III. at maximum Cp, the local blade angle-of-attack at, and inboard of the 80% radial station remains broadly constant α=6.6° until the 40% station is reached;
IV. the point of maximum power production is consistent with local blade operation at optimum efficiency (max LD, α=6.6°) for a well designed rotor.

3.2.3 Rotor Blade Grid Convergence

A grid convergence study is now presented to establish solution independence from mesh resolution. To remain consistent with meshing strategies planned for the composite rotor geometry and flume test case, the present grid convergence study is conducted for a unit span aerofoil using a three-dimensional fully unstructured grid.

Blade operating conditions for the grid convergence study are informed by both predictions of rotor performance via the blade element study (Section 3.2.1) and a description of the hydraulic environment (Section 2). This corresponds to a chord Reynolds number of Re~42,000 at an angle of attack of α=6.6° (Figure 3.2.4) for the rotor operating at a tip-speed-ratio corresponding to its maximum (unbounded) power coefficient within the *U0, T0* flow-field. Transforming the base-line turbulence intensity readings, taken by EDF and reproduced here in Figure 2.1.2, into a blade fixed rotating frame enables the calculation of incident blade turbulence intensity representative of the flume environment. Figure 3.2.6

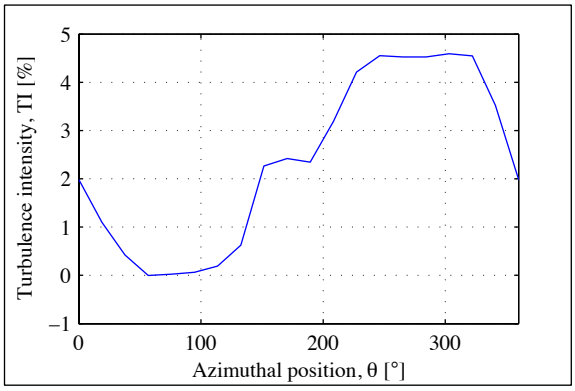

Figure 3.2.6: Incident blade fixed turbulence intensities at an 80% radial station (*U0, T0*).

illustrates the variation of blade fixed turbulence intensity at an 80% radial station. Here, a sinusoidal type variation of turbulence intensity corresponding to the blades position within the flume's boundary layer is observed. An azimuthal position of θ=90° relating to blade top dead centre, external to the boundary layer, and a position of θ=270° relating to blade bottom dead centre, deep within the boundary layer close to the tunnel floor. An average inflow turbulence intensity of TI=2% is selected for the grid convergence tests in light of the blade relative turbulence intensities shown in Figure 3.2.6.

Resolution	Total cell #	Maximum blade surface cell dimension [xc^{-1}]
Course	108,000	0.20
Medium	115,000	0.16
Fine	172,000	0.12

Table 3.1: Overview of grids used within blade convergence study.

Table 3.1 summarizes total cell count and maximum blade surface cell dimension for the three grid resolutions trialled. For all of the grids, resolution close to the leading and trailing edges was set to twenty times the maximum blade surface cell dimension. An illustrative example showing the surface grid for the medium resolution test case is presented in Figure 3.2.8. Boundary layers are resolved using a stack of six high aspect ratio prismatic cells. The first surface cell height is set to y_1=3x10^{-4} [ms^{-1}] after which a geometric growth factor of

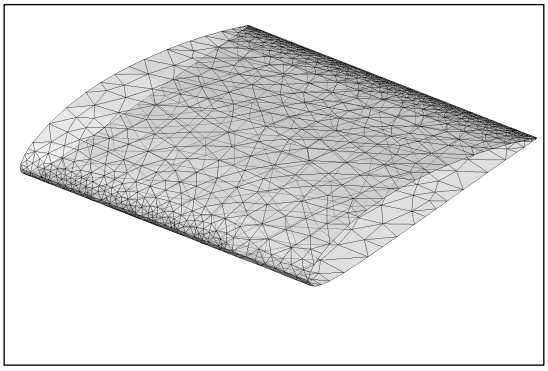

Figure 3.2.7: An illustrative example showing blade surface mesh for the medium-resolution grid.

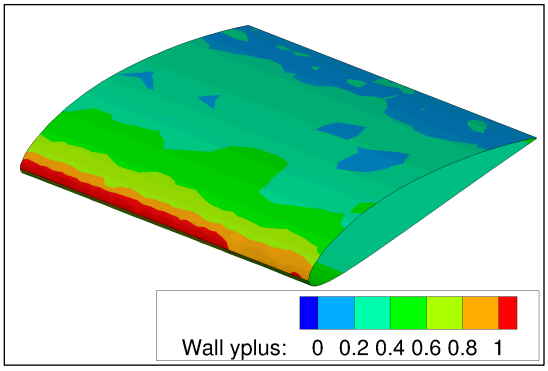

Figure 3.2.8: An illustrative example showing blade surface y^+ for the medium-resolution grid (α=7.0°).

gf=1.2 is used to inflate the cell dimension in the wall normal direction. A confirmation of resolution of the viscous sub-layer is provided by Figure 3.2.8 showing values of y^+<1 across the majority of the blade chord at an angle of attack close to the aerofoil's maximum lift to drag operating point (α=7.0°).

Preliminary investigations employing various turbulence closure models (k-ω SST, k-kl-ω and Transition SST) indicated only minor differences for flows comprising an inflow turbulence intensity of 2%. The two equation k-ω SST

model is therefore favoured over the three equation k-kl-ω and four equation Transition SST for arguments grounded on computational cost.

Figure 2.1.1 presents lift/drag polars for the three grid resolutions trialled for an angle of attack range from α=-6.0° to α=12.0° in 1.0° increments. Each successive grid resolution is shown to produce very similar lift-drag characteristics suggesting a numerically converged stencil. Examination of the maximum lift to

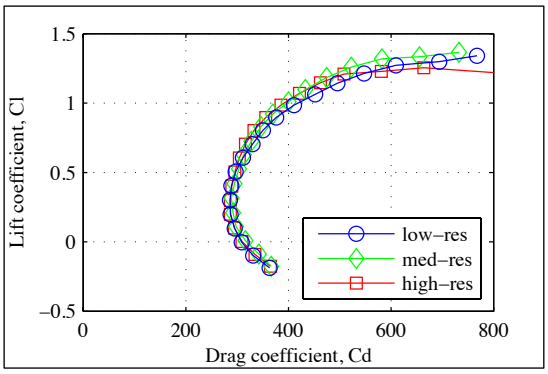

Figure 3.2.9: A demonstration of grid convergence illustrating the full drag polar for three levels of mesh refinement (unit span NACA-4415, Re:4.2e⁴, -6.0°<α<12.0°).

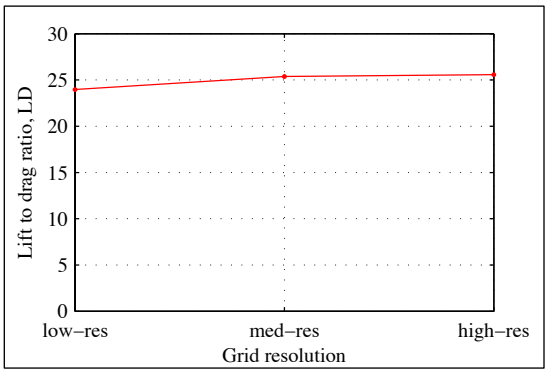

Figure 3.2.10: A demonstration of grid convergence illustrating lift to drag ratio across three levels of mesh refinement (unit span NACA-4415, Re:4.2e⁴, α=7.0°).

drag ratio (α=7.0°) in Figure 3.2.10 further demonstrates numerical convergence, showing a change in lift to drag ratio of less than 6.5% moving from the high to the low resolution grid.

3.2.4 Validation of Rotor Blade Model

Comparisons between predicted blade forces and wind tunnel data are presented to further validate the rotor blade component model in Figure 3.2.11. Agreement in the high lift-to-drag region is shown to be excellent. Disparities exist at lower lift coefficients. This is considered due to a lack of transition model within the k-ω SST turbulence model. However, it has been shown in Section 3.2.1 that a robust prediction of blade loads in the low lift region is unnecessary for performance predictions close to the maximum power performance point and Figure 3.2.11 is considered to provide an effective validation of the high-resolution rotor blade grid.

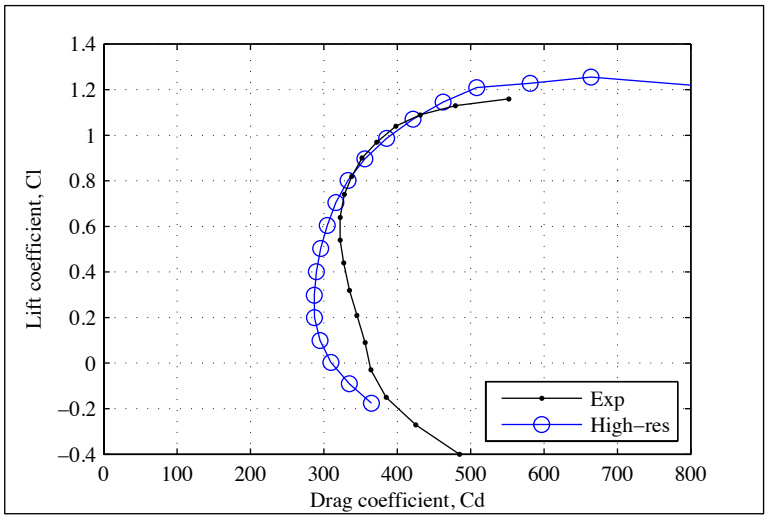

Figure 3.2.11: Comparison of experimental wind tunnel data Miley (1982) with computational predictions using the high-resolution grid

(unit span NACA-4415, Re:4.2e^4, -6.0°<α<12.0°).

3.3 Rotor Tower Component Validation

Support for the turbine assembly is provided by a surface piercing cylindrical tower. Connected to the nacelle ~2/3 of a radius downstream of the rotor plane (Figure 3.1.1), this tower presents an obstruction to the flow resulting in an increase in static pressure and decrease in flow velocity upstream of the body. The flow field perturbation ahead of the support tower will extend far upstream and will consequently interact with the rotor blades. As such, there is a requirement to verify the correct simulation of the flow-field surrounding the tower component.

In the range of Reynolds numbers, Re_D based on tower diameter *D*, at which the experiments will be conducted, the tower will form a turbulent wake even in otherwise unperturbed, i.e. laminar, approach flow. The location of the boundary layer separation points has a direct effect on the width of the wake; early separation results in a wide wake and late separation results in a narrow wake. The profile drag of the cylinder increases with wake width; and increased drag results in a greater change to the pressure and velocity fields upstream of the cylinder (by conservation of linear momentum).

The rotor blades will pass directly through the region of perturbed pressure and velocity upstream of the tower, altering the local flow speed and angle of

incidence seen by the blades from those observed in the absence of the tower. Hence, it is imperative that the flow past the tower, and particularly the drag exerted on the tower, is properly modelled in order that the flow environment seen by the rotor blades is properly represented.

3.3.1 Flow Past Cylindrical Bodies

The flume experiments are carried out for two flow conditions, *U0* and *U1* (each identified by a reference velocity and turbulence intensity profile). The rotor will act to extract momentum from the flow such that the approach velocity seen at the tower will be reduced below that observed far upstream of the rotor. The reduced velocity is estimated at 2/3 of the upstream velocity. This estimate is based on the velocity decrement through an ideal axial-flow turbine operating close to maximum power in an unconstrained flow. The Reynolds number, based on a tower diameter of 0.04 m, is calculated based on reduced approach velocity at the tower as follows:

Flow Condition	**Upstream reference velocity, U_∞ [m/s]**	**Tower approach velocity, U_t [m/s]**	**Tower Reynolds number, Re_D**
U0	0.27	0.18	7190
U1	0.55	0.37	14640

Table 3.2: Reynolds numbers for flow conditions *U0* and *U1*.

where the tower Reynolds number is defined as:

$$\mathrm{Re}_D = \frac{U_t D}{\nu}, \qquad \textbf{(3.1)}$$

and ν is the kinematic viscosity of water.

The Reynolds numbers calculated above indicate that, for otherwise undisturbed approach flow, the flow past the tower will remain sub-critical with laminar boundary layers, laminar separation points and transition to turbulence in the free-shear layers, which will roll up to form turbulent vortex structures shed alternately from either side of the cylinder, resulting in a classical von Kármán type wake.

The alternate vortex shedding generates mean and fluctuating forces on the cylinder, conventionally resolved into lift and drag components, perpendicular and parallel to the approach flow respectively. The lift and drag forces vary sinusoidally, with the drag force fluctuating at twice the frequency of the lift force. Three-dimensional instabilities generally cause the phase of the vortex shedding to vary along the length of the cylinder. The sectional lift and drag coefficients are defined by:

$$C_L = \frac{f_y}{\frac{1}{2}\rho U^2 D}; C_D = \frac{f_x}{\frac{1}{2}\rho U^2 D}; \quad \textbf{(3.2)}$$

where f_x and f_y are the stream-wise and cross-stream forces per unit cylinder span, and *U* is the appropriate approach velocity. The vortex shedding frequency, f_s, is represented through the non-dimensional Strouhal number, St

$$St = \frac{f_s D}{U}, \quad \textbf{(3.3)}$$

and the pressure coefficient, C_p

$$C_p = \frac{p - p_\infty}{\frac{1}{2}\rho U^2}, \quad \textbf{(3.4)}$$

where p_∞ is the upstream static pressure.

3.3.2 Turbulence Models Applied to Cylinder Flows

The Reynolds-averaged Navier-Stokes (RANS) equations are not in themselves solvable without specification of the eddy viscosity. Conventionally, one of a variety of turbulence models is employed to close the system of RANS equations. In the present investigation the choice of turbulence model is driven primarily by its effectiveness in capturing the flow field around the rotor blades. However, as noted above, accurate calculation of the flow field around the tower, and more specifically the drag force acting on the tower, is also important.

Another aspect of the turbulence model to be considered is the extra computational load caused.

The primary objective of the tower component validation exercise is to determine the most appropriate grid and turbulence model to use. By their nature, RANS solvers are unable to simulate three-dimensional phasing effects and hence the calculation of C_D, C_L, C_p and St can be carried out as effectively through two-dimensional simulation, with great savings of computational effort.

Numerical simulations with various turbulence models have been carried out on a two-dimensional circular cylinder. A diameter of 0.04m has been chosen, corresponding to the greater portion of the turbine tower. The Reynolds number is set at 10,000, for direct comparison with available published experimental and numerical data. An example of the computed flow-field, here shown for the k-w model, is shown in Figure 3.3.1.

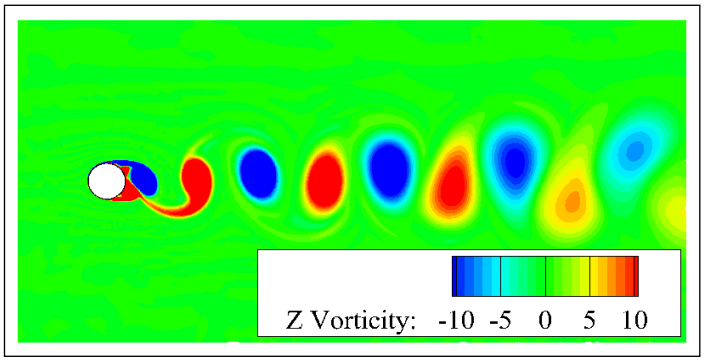

Figure 3.3.1: Contours of *z*-vorticity highlighting vortex shedding from cylinder.

The effectiveness of a particular turbulence model is determined by calculation and comparison to experiments of certain flow-field properties. Tabulated below are computed results from selected turbulence models along with corresponding values from Direct Numerical Simulations (DNS) and experiments. For the present simulations the time-step, Δt, is 0.005 seconds. The cells adjacent to the cylinder have a y^+ height on the order of one for full resolution of the boundary layer.

		C_{Dmean}	C_{Lrms}	St	$-C_{pb}$
Present simulations	k-w-SST	1.685	0.128	0.247	2.114
	k-kl-w	1.142	0.517	0.257	1.043
	Transition-SST	1.582	1.153	0.229	-
	k-e	0.864	0.135	0.199	-
DNS	Dong (2005)	1.143	0.448	0.203	1.129
Experimental	Gopalkrishnan (1993)	1.186	0.384	0.193	-
	Williamson (1996)	-	-	-	1.112

Table 3.3: Comparison of simulations with published experimental and numerical data.

Characterizing $-C_{pb}$ as the base pressure coefficient, measured 180° aft of the mean stagnation point. This variable is representative of pressure drag but more sensitive to subtle changes than the drag coefficient itself.

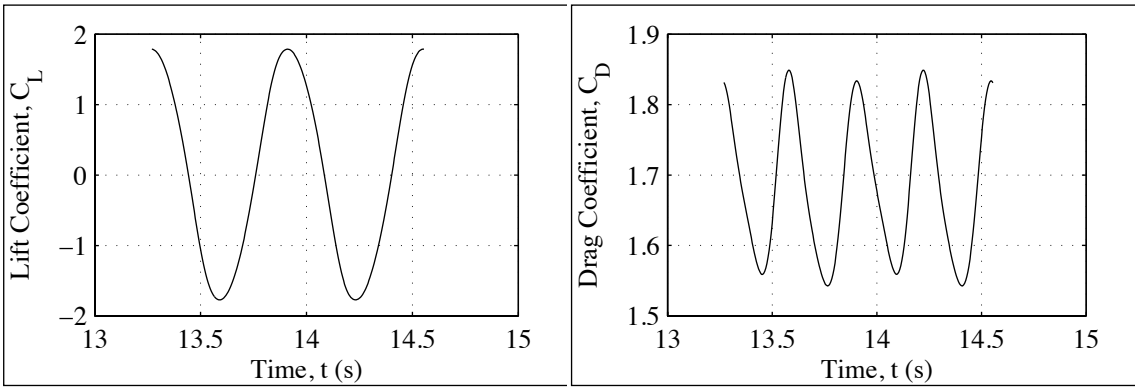

(a) Lift coefficient. **(b) Drag coefficient.**

Figure 3.3.2: Illustrations of force coefficient histories for two full vortex- shedding cycles.

Of the four turbulence models under examination, the k-kl-ω model generally yields the most favourable results. Note however that the drag and lift coefficients are integral statistics, and may mask localised flow effects such as the position of separation. The distribution of pressure along the cylinder surface is a useful indicator of boundary layer separation and wake width. In Figure 3.3.3 below, the time mean pressure coefficient, C_p, is plotted as a function of azimuthal angle over one side of the cylinder, from stagnation point (0˚) to base point (180˚) for the k-ω SST and k-kl-ω models. Also shown in the figure are experimentally determined pressure distributions from Thom (1928) and Linke (1931).

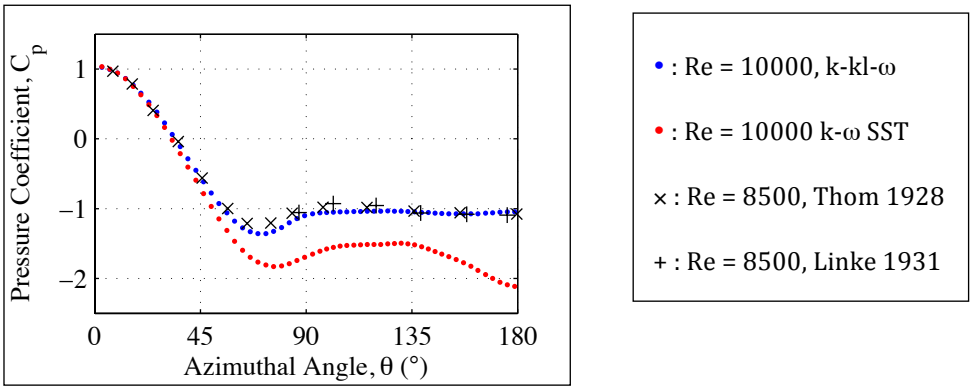

Figure 3.3.3: Pressure coefficient distribution around the cylinder.

It is clear from the pressure distributions that the k-kl-ω model continues to compare well with experimental data. Its success lies in its ability to capture locally laminar flow early on in a developing boundary layer, before 'switching on' a turbulence model as the boundary layer makes the transition to turbulence.

3.3.3 Cylinder Grid refinement

Grid refinement studies have been carried out for both the k-ω SST and k-kl-ω models to ensure the solutions obtained are numerically converged. A series of three grids were used, with global resolution approximately increasing by a factor of four (grid resolution increased by a factor of two in a circumferential and wall normal sense, holding the wall-adjacent cell height constant) from grid to grid. In each case the cells adjacent to the cylinder surface were of wall normal

height, $\delta n = 4.08 \times 10^{-5}$ m (or $\delta n / D = 1.02 \times 10^{-3}$), corresponding to a y^+ range of 1.0 to 7.0.

Grid	Number of circumferential cells	Circumferential cell dimension ($\delta s / D$)	Total number of cells
1	60	0.0167	5595
2	114	0.0088	19612
3	234	0.0043	77467

Table 3.4: Description of grid series.

The resolution study showed that the k-kl-ω model is in fact not well-suited to separated flow problems. Whilst excellent results are produced for the coarser grids, the model fails to simulate an unsteady flow field, i.e. vortex shedding, at the highest resolution. Away from the near wall regions, the k-kl-ω scheme uses a k-ω turbulence model, which is overly dissipative and hinders the development of unsteady flow around the cylinder. In contrast, the k-ω SST turbulence model employs a k-ε model outside of the near-wall regions, which is less dissipative and does not suppress vortex shedding as resolution is improved.

3.3.4 Summary and Implications of Cylinder Component Modeling

In selecting the turbulence model it should be noted that a single turbulence model must be used throughout the computational space and hence a compromise may have to be sought in which the selected turbulence model works well for some aspects of the flow field and less well for others. We select the k-ω SST model over the k-kl-ω model for two reasons. Firstly, after a component-level analysis of the rotor blades, the k-ω SST model was found to yield better results than the k-kl-ω model. Accurate modelling of the rotor must take precedence over accurate modelling of the tower.

Secondly, as highlighted in Section 3.3.2, the effectiveness of the k-kl-ω turbulence model in capturing the unsteady flow field around the cylinder is reduced with increasing resolution. This type of behavior, in which an increase in

numerical dissipation deteriorates the solution quality and in this case alters the gross flow features, is an undesirable characteristic that is to be avoided at all costs.

However, from the results presented in Figure 3.3.3, it is evident that there is considerable error between the k-ω SST turbulence model ($C_{Dmean} = 1.685$) and experimental data ($C_{Dmean} = 1.186$, Gopalkrishnan 1993). Such error must be compensated for in an acceptable manner.

The most significant influence of the tower on the flow field is the effect it has on the pressure and velocity fields upstream at the rotor plane. The increase in static pressure and decrease in stream-wise velocity are caused primarily by the drag of the tower (by conservation of linear momentum). It is therefore most important that the tower drag and not the sectional drag coefficient *per se* be computed correctly. An appropriate mechanism to ensure that the k-ω SST model simulates the tower drag correctly, despite over predicting the sectional drag coefficient, is to modify the tower diameter. Equating the computed drag force with that required:

$$f_x = C_{Dcomputed} \frac{1}{2} \rho U^2 D_{computed} = C_{Dactual} \frac{1}{2} \rho U^2 D_{actual} \qquad \textbf{(3.5)}$$

where $C_{Dactual}$ and D_{actual} are set to the experimentally expected mean drag coefficient ($C_{Dactual} = C_{Dmean} = 1.186$) and the actual diameter of the tower ($D_{actual} = D = 0.04\,\text{m}$). Noting that drag force is linearly related to cylinder diameter allows:

$$D_{computed} = D_{actual} \frac{C_{Dactual}}{C_{Dcomputed}} \qquad \textbf{(3.6)}$$

where $D_{computed}$ is the tower diameter required in the numerical simulations to ensure that the drag force is properly modelled and $C_{Dcomputed} = 1.685$ is the drag coefficient computed with the k-ω SST model. In all simulations presented in this report the tower diameter has been appropriately modified as outlined above, downscaled to ~70% of the actual tower diameter.

4 Composite Simulation

Following on from a successful component-by-component verification of all fluid-dynamically significant parts in Sections 2 and 3 a composite model of the rotor assembly within a section of the EDF flume is now constructed. An overview of the three-dimensional meshing strategy and computational setup is given in Section 4.1 and Section 4.2. A single tip-speed-ratio calculation is then run and analyzed in Section 4.3.

4.1 Meshing Strategy

Consistent with the grid convergence studies presented for the unit span NACA 4415 aerofoil in Section 3.2, a fully unstructured mesh incorporating tetra volume elements is employed for the composite simulation. Blade surface grid resolution is informed by the high-res grid convergence case presented in Section 3.2. A grid refinement of ~20 times the maximum blade surface cell width is used to resolve the blade leading and trailing edges. Similar resolutions with curvature-based refinement are used for the hub, nacelle and tower. Illustrative examples of the resulting surface mesh for the rotor assembly are presented in Figure 4.1.1 and Figure 4.1.2.

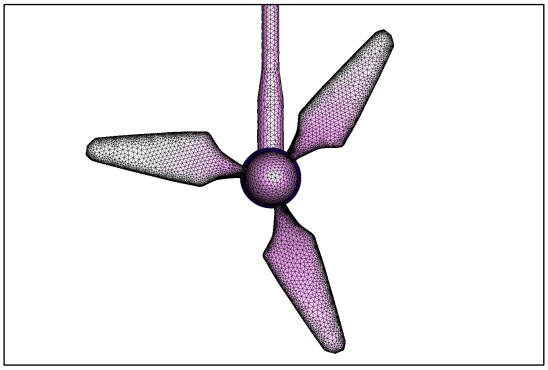

Figure 4.1.1: A detailed graphic illustrating the front view of the blade, tower and hub mesh.

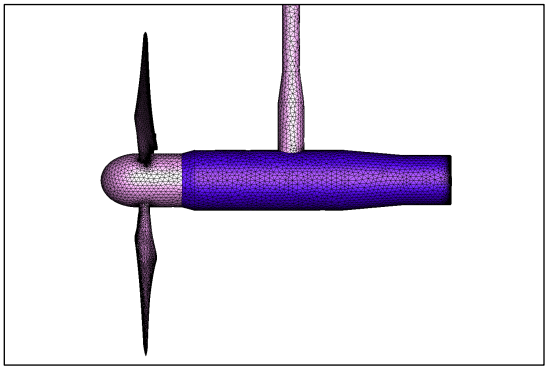

Figure 4.1.2: A detailed graphic illustrating the side view of the blade, tower, nacelle and hub mesh.

The boundary layers for the components shown in Figure 4.1.1 and Figure 4.1.2 are fully resolved with the first cell height resulting in a y^+~1. Eight prismatic inflation layers are used to capture the boundary layer with a growth factor of gf=1.2.

The rotation of the turbine blades / hub is accommodated within the composite model through the use of a sliding mesh. Figure 4.1.3 illustrates this 'coin type' sliding mesh interface encompassing the rotor blades and hub. At the start of each time step dt all mesh within the coin rotates ωdt about the hub axis, where ω is defined as the rotational speed of the rotor. Thus simulating blade/hub rotation with respect to the fixed walls, floor, nacelle and tower.

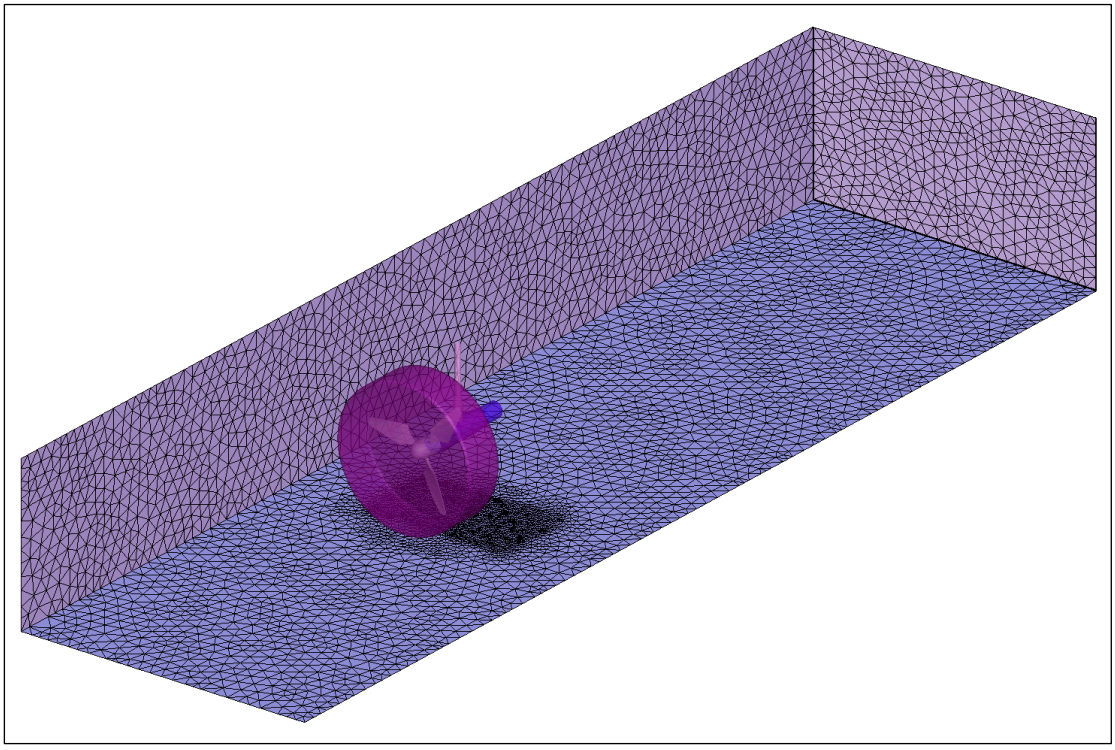

Figure 4.1.3: An illustration of the flume computational domain showing turbine placement, flume walls and the 'coin type' sliding mesh interface encompassing the rotating blades.

A high-resolution mesh region adjacent to the rotating coin, visible along the floor surface in Figure 4.1.3, is utilized to limit artificial numerical dissipation close to the rotor plane. The flume domain extends three rotor diameters upstream and six rotor diameters downstream of the rotor plane.

Boundary layers along the flume floor and sidewalls are modelled using wall functions. Prismatic layers are again used in these regions, however with an increased first cell height corresponding to a y^+~100 inflated in the wall normal direction over four layers with an growth factor of gf=1.2.

The full composite mesh contains ~3 million tetrahedral elements.

4.2 Computational Setup

To demonstrate model functionality, a single tip-speed-ratio case of $\lambda \sim 3.5$ is run. This tip-speed-ratio is coincident with the operating point resulting in maximum performance of the unbounded rotor presented in Section 3.2.1. Serving as a frequently reported metric characterising turbine performance, verification at this maximum power operating point is considered sufficient for the demonstration of model functionality. A uniform inflow of u=0.27ms^{-1} is set along inflow plane along with a uniform turbulence intensity of TI=5% and a uniform length scale of l=0.2m*. This inflow boundary condition is similar to the *U0, T0* test case. A closer representation of the *U0, T0* inflow, including velocity and turbulence intensity profiles as presented in Section 2, is planned for future comparative tests with experiment. At the point of writing, the baseline flow-field remains subject to change (as discussed in Section 2.1.2) and a uniform inflow condition is considered sufficient for the purpose of model demonstration. The water surface is currently modelled as a rigid lid employing a slip condition. Further comparative tests and all future deliverables will employ the Volume of Fluid UDF presented in Section 2.3 to model the free surface.

Once initialized, the unsteady solution is stepped forward in time. A step size of dt=0.0066 [s] is used, with ~302 time steps completing a full revolution. A total of 15.6 revolutions are simulated in order to attain a temporally converged solution.

A selection of unsteady force traces and flow field slices are now presented below in Section 4.3. The following data set is the result of a 36 core submission executed for a total of ~144 wall clock hours.

* Previous analysis of the flume environment indicated an average turbulent length scale of l=0.2m. Values of turbulent length scale commensurate with improved analysis of the flume environment, such as that given in Figure 2.1.6, shall inform future simulations.

4.3 Flow Field Analysis

Figure 4.3.1 illustrates the unsteady rotor power coefficient over five full revolutions from rotation number 10 to 15. This power coefficient is calculated as a sum of the rotor blade and hub torque coefficients taken about the rotor axis and multiplied by tip-speed-ratio,

$$C_p = \lambda C_t, \tag{4.1}$$

All coefficients are normalized by inflow dynamic pressure and rotor area. Temporal convergence is demonstrated over the five revolutions shown, C_p oscillating about a mean value of $\overline{C_p} = 0.51$ with a standard deviation of $\sigma = 0.51\%$. The simulated mean power coefficient is significantly larger than the blade element model prediction calculated in Section 3.2.1, $\overline{C_p} \approx 0.4$. A blockage effect, with the rotor occupying ~24% of the flume cross-section is the likely cause of this increase in performance over the BEM prediction for unbounded flow.

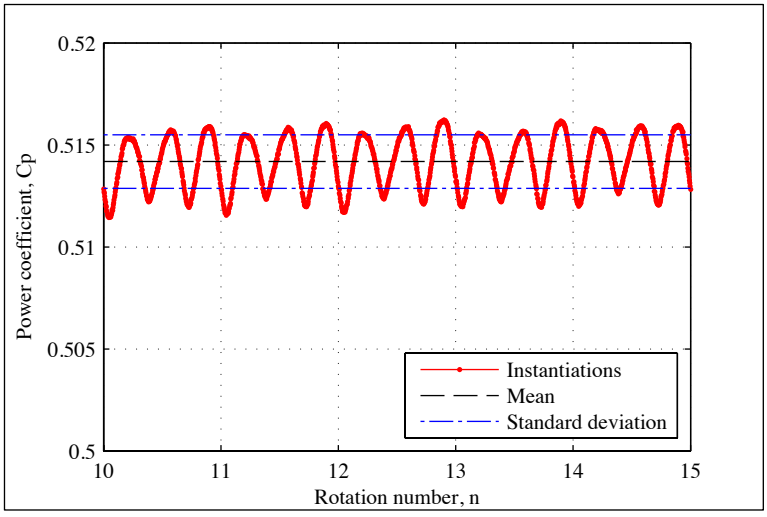

Figure 4.3.1: An illustration of unsteady power coefficient extracted from the sum of torques applied to all three turbine blades and hub.

Figure 4.3.1 clearly shows a dominant frequency equal to three times the turbine's rotational frequency. At the start of each revolution one rotor blade is

aligned with the support tower pointing vertically upwards. Just past the start of each revolution and again shortly after 120° and 240° into each revolution a minimum in power coefficient is observed. Here, the upstream influence of the tower is considered responsible for the slight decrease in power; the high-pressure region upstream of the tower reduces the pressure difference maintained across the passing blade. In addition to the three times per revolution forcing, there appears to be a once-per-revolution component. The mechanism for this fluctuation is not currently understood.

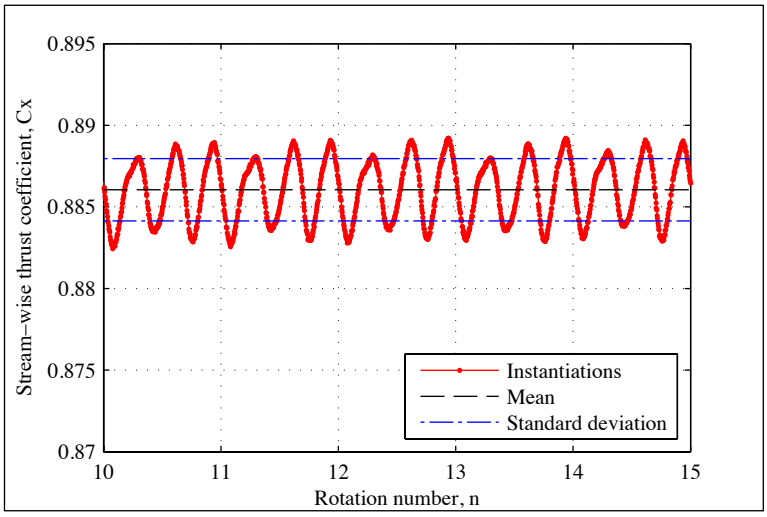

Figure 4.3.2: An illustration of unsteady stream-wise thrust coefficient extracted from the sum of forces applied to all three turbine blades, hub and nacelle.

Figure 4.3.2 illustrates the corresponding unsteady stream-wise force trace. Both the dominant three-per-revolution and secondary once-per-revolution components are again clearly visible with the three-per-revolution component attributed to tower passing. A standard deviation of $\sigma = 0.43\%$ is calculated for the stream-wise force fluctuations.

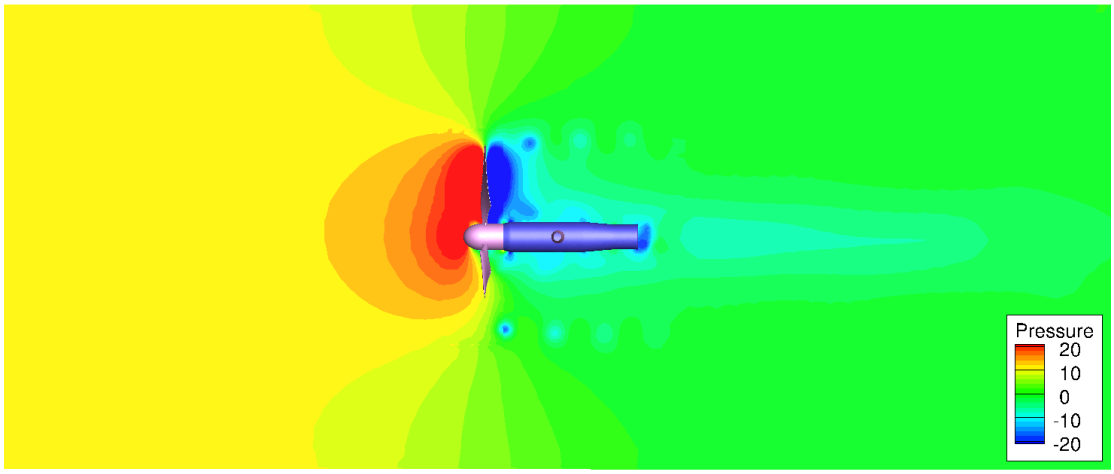

Figure 4.3.3: An illustration showing instantaneous contours of static pressure taken along a horizontal slice aligned with the flume centerline (λ=3.5, U0, T0).

Figure 4.3.3 illustrates contours of instantaneous static pressure shown along a horizontal centerline slice through the computational domain. A pressure jump from high to low applied across the rotor in the stream-wise sense is clearly visible. This pressure jump is primarily responsible to the high stream-wise thrust coefficients presented Figure 4.3.2 and is also an necessary requirement for power extraction using axial flow turbines. Due to the instantaneous nature of the pressure field presented in Figure 4.3.3, a larger pressure jump is observed in the upper half of the image, where a blade is almost intersecting the horizontal plane, than in the lower half of the image. Also visible in Figure 4.3.3 are a number of low-pressure circular regions, attributed here to tip vortices shed from each of the turbine's three blades.

Figure 4.3.4 illustrates velocity magnitude taken on a horizontal plane placed 1/3 of a radius above the rotor centerline. Pertinent features of this image are: the deceleration of the flow passing through the rotor plane, indicative of both momentum and power extraction from the free stream; flow blockage effects,

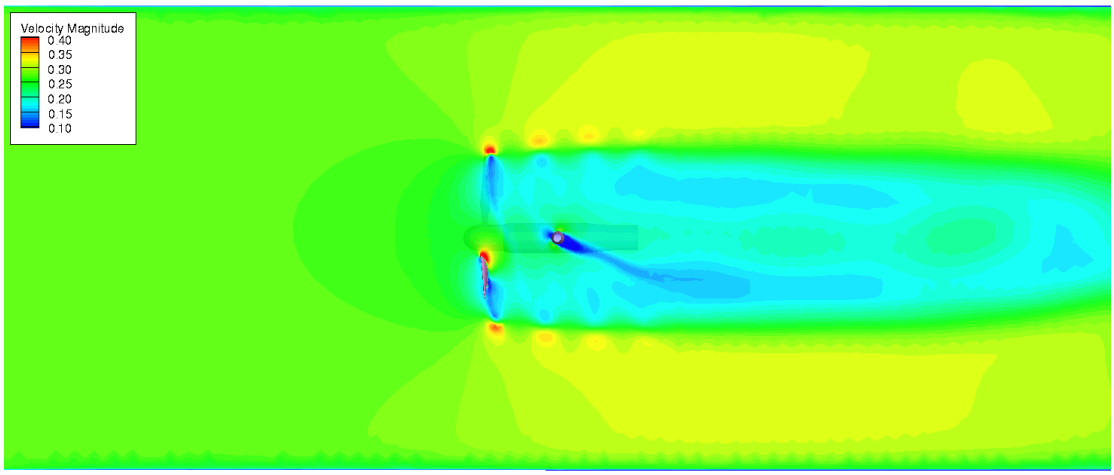

Figure 4.3.4: An illustration showing instantaneous contours of velocity magnitude taken along a horizontal slice placed 1/3 of a radius above the flume centerline (λ=3.5, U0, T0).

suggested by a mean power coefficient higher than predicted by BEM models, clearly visible in the form of an accelerated flow field either side of the low velocity core; the presence of a helical tip vortex rolling up from each of the rotor blades; and an inclination of the tower wake away from the stream-wise direction, which is a result of swirl imparted to the flow by the rotor. The observed inclination of the tower wake will vary along the tower length due to radial variations in blade loading and also a function of tip-speed-ratio. This observation has obvious implications for any faired-tower designs. The inclination of the tower flow-field and associated upstream high-pressure region is considered the cause of the slight offset between blade zenith and the angular location of maximum blade-tower interaction; indicated in Figure 4.3.1 and Figure 4.3.2 by minima in the unsteady force and power traces.

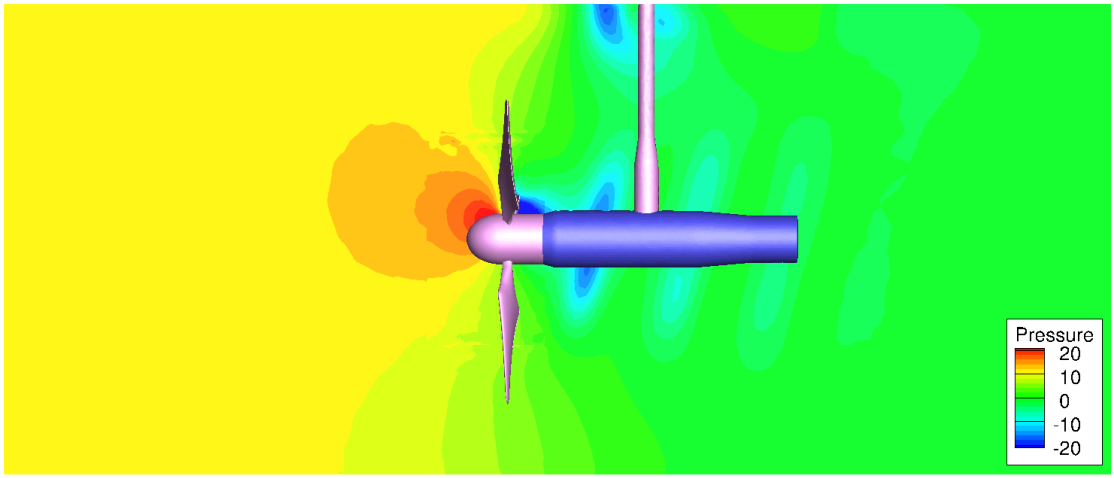

Figure 4.3.5: An illustration showing instantaneous contours of static pressure taken along a vertical slice offset one radius beyond the flume centerline (λ=3.5, U0, T0).

Figure 4.3.5, Figure 4.3.6 and Figure 4.3.7 illustrate instantaneous contours of static pressure shown on vertical planes aligned with the rotor axis with radial offsets of -1R, 0 and 1/3R respectively.

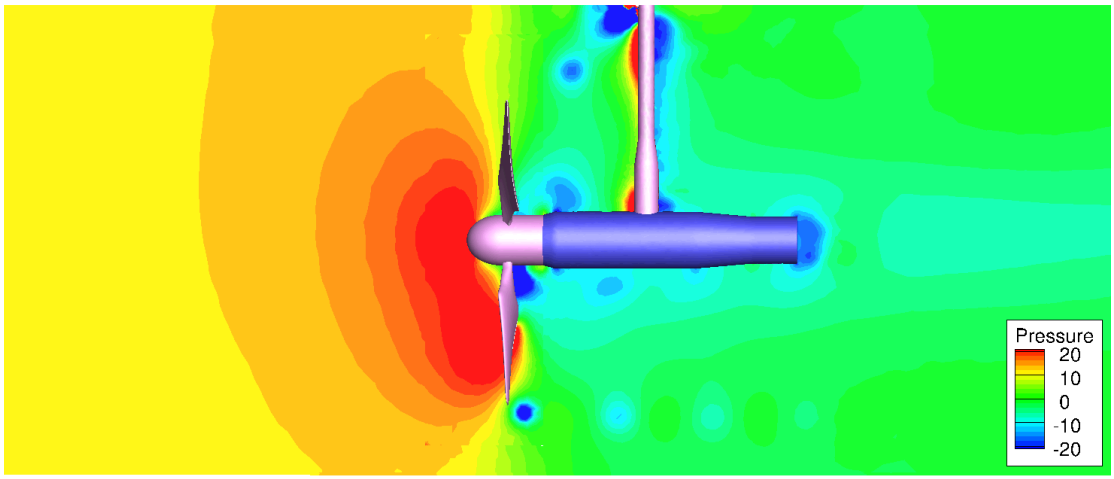

Figure 4.3.6: An illustration of static pressure contours taken along a vertical slice coplanar with the flume centerline (λ=3.5, U0, T0).

Figure 4.3.5 highlights the high-pressure and low-pressure regions either side of the far blade tip intersecting with the plane. Additionally, a number of low-pressure strips visualize the helical tip vortices present in this region.

The centerline slice presented in Figure 4.3.6 clearly shows a large pressure jump across the rotor along with both tip vortices (see previously) and a number of low-pressure circular regions in close proximity to the turbine nacelle

consistent with low pitch hub vortices. The pressure differential applied across the tower is visible in this image as is a low-pressure region at the rear of the nacelle.

Figure 4.3.7 illustrates a pressure plane intersecting two rotor blades. Again the pressure differential across the rotor plane and helical tip vorticity are both visible.

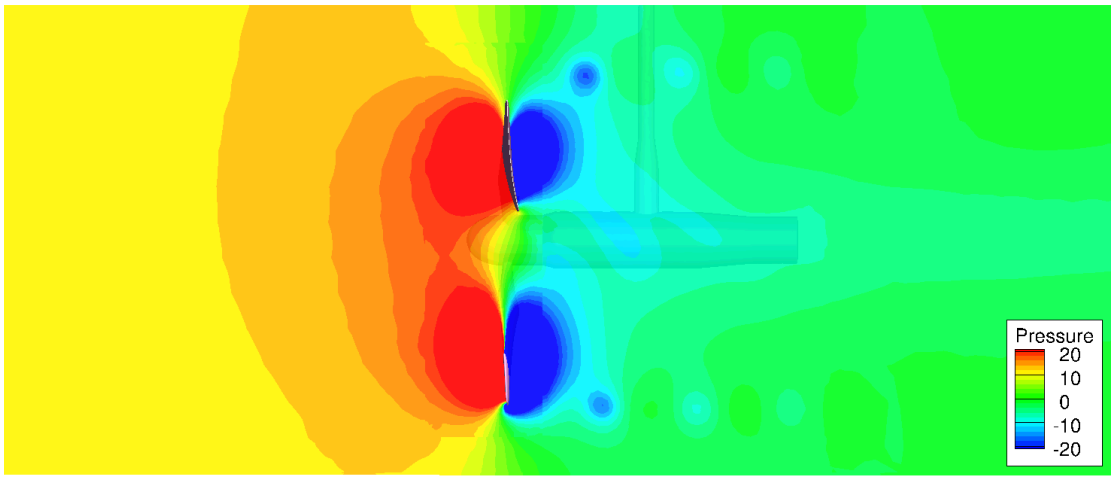

Figure 4.3.7: An illustration showing instantaneous contours of static pressure taken along a vertical slice offset 1/3 of a radius ahead of the flume centerline (λ=3.5, U0, T0).

Figure 4.3.8 presents an isometric projection of the rotor assembly illustrating both a number of instantaneous stream-tracers visualising the velocity field and a vorticity $|\omega|=6.0$ $[s^{-1}]$ magnitude iso-surface coloured with contours of static pressure.

The stream-tracers primarily highlight the transfer of angular momentum by the rotor to the fluid causing the wake to swirl and generating the local flow-field inclination observed for the tower in Figure 4.3.4. In regions where the stream-traces are observed to pass close to the helical tip vortices a Prandtl type interaction is observed.

The vorticity iso-surfaces clearly visualize the rollup of blade vorticity shed along the trailing edge into a consistent helical vortex system or tip vortex. The presence of hub vortices, suggested by a number of low-pressure regions in Figure 4.3.6, is confirmed by Figure 4.3.8. Here, a set of three high-pitch helical hub vortices are clearly visible.

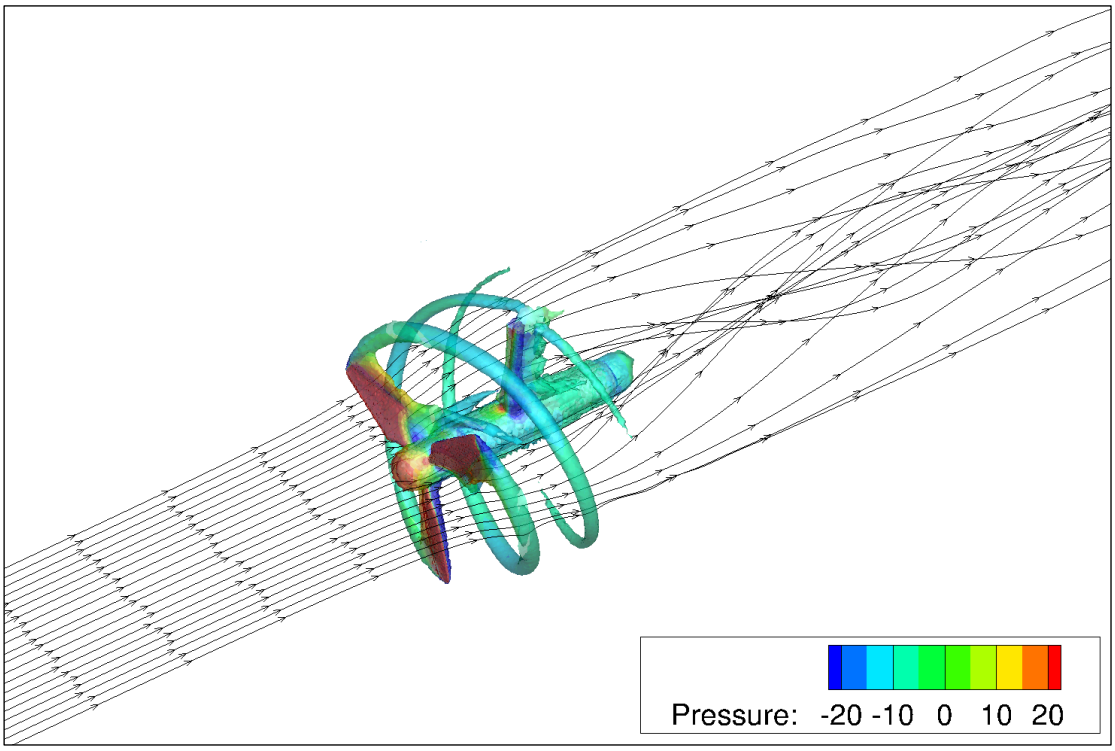

Figure 4.3.8: A composite illustration showing a set of stream-tracers imposed on the instantaneous velocity field along with iso-vorticity contours $|\omega|=6.0s^{-1}$ coloured by contours of instantaneous static pressure ($\lambda=3.5$, U0, T0).

Pressure contouring along the vorticity iso-surface highlights high-pressure regions along the support tower, close to the centre of the hub and across the upstream-facing blade surfaces. Low-pressure regions are observed along the vortex cores and down-stream of the tower.

5 Conclusions

The verification of model structure and operation has required a multi-level approach, summarized as follows:

I. The flume environment

Successful comparison between experiment and computation relies on a clearly defined baseline flow environment. Parameterization and simulation of the bare flume highlights the following pertinent points:

a. analysis of the low flow rate *U0,* low turbulence intensity *T0* experimental test case has produced well defined velocity and turbulence intensity profiles;
b. the rotor plane flow-field for the *U0, T0* case is observed to be both readily parameterized and is considered to be physically representative of low turbulence intensity full-scale tidal flows;
c. overall velocity profiles for the *U0, T0* case are well represented by a 13^{th} power-law, with velocity variations close to the wall better handled by a log-law variation with a roughness height of z_o=3.21x10^{-6} [m];
d. an ancillary User Defined Function UDF is successfully developed, validated and combined within the FLUENT environment for the correct simulation of free-surface flows containing tidal turbines.

II. Component-by-component verification

Complexity implicit within the full three-dimensional turbine model necessitates a component-by-component verification, including validation with experimental data wherever possible. A summary of this procedure is detailed as follows:

a. whilst tower computations achieved very good agreement using a transitional turbulence model (k-kl-ω), the use of the 'fully

turbulent' k-ω model (dictated by blade requirements) resulted in an over prediction in drag;

b. effective tower drag using the k-ω model was matched to experimental predictions via a 30% reduction in diameter;
c. unit span blade simulations where found to match experimental data well, with results from a grid convergence study informing the generation of the full rotor mesh.

III. Full rotor simulation

Information gained from analysis of the flume environment and the component-by-component study enabled the generation of a physically sound numerical representation of the flume-scale experiment. A test case run at a tip-speed-ratio of λ=3.5 highlighted a number of interesting flow features:

a. a mean power coefficient of C_p=0.51 is attained for a tip-speed-ratio of λ=3.5;
b. the increase in simulated power coefficient above BEM predictions is considered due to favorable flume blockage effects.
c. tower-turbine interaction generates three-times-per-revolution unsteady components in power and stream-wise force, with respective fluctuation amplitudes of 0.51% and 0.43%;
d. swirl downstream of the rotor plane generates an inclined flow-field incident to the turbine tower, varying with height and tip-speed-ratio, that would effectively prevent any attempt to fair the tower of axial flow tidal turbine devices;
e. swirl down stream of the rotor plane introduces a small time offset in the tower-turbine power and thrust histories with respect to tower-blade passing.

References

BUVAT, C. & MARTIN, V. (2010). Identification of Test Requirements and Physical Model Design, PerAWAT WG4 WP1 D1 v3.0. *EDF - Recherche et Développement, 6 Quai Watier, 78401 CHATOU Cedex, France.*

BUVAT, C. & PEYRARD, C. (2010). Calibration Tests Without Turbine, PerAWAT WG4 WP1 D3 v0.1. *EDF - Recherche et Développement, 6 Quai Watier, 78401 CHATOU Cedex, France.*

DONG, S. (2005). DNS of Flow Past a Stationary and Oscillating Cylinder at Re = 10000. *Journal of Fluids and Structures,* **20,** 519 – 531.

DUNCAN, W.J., THOM, A.S. & YOUNG, A.D. (1970). *Mechanics of Fluids.* Arnold, 2nd edn.

FERRER, E., & MUNDUATE, X. (2007). Wind Turbine Blade Tip Comparison Using CFD. *The Science of Making Torque from the Wind*. Journal of Physics, Conference Series, 75.

FRERIS, L.L. (1990). *Wind Energy Conversion Systems*. Prentice Hall.

GOPALKRISHNAN, R. (1993). Vortex-Induced Forces on Oscillating Bluff Cylinders. *Ph. D. Thesis, Department of Ocean Engineering, MIT, Cambridge, MA, USA.*

HOULSBY, G.T., DRAPER, S. & OLDFIELD, M. (2008). *Application of Linear Momentum Actuator Disc Theory to Open Channel Flow*. Technical Report 2296-08. University of Oxford.

LINKE, W. (1931). Neue Messungen zur Aerodynamik des Zylinders, insbesondere seines reinen Reibungswiderstandes. *Physikalische Zeitschrift,* **32**, 900 – 914.

MASSEY, B. S. (1983). *Mechanics of Fluids, 5th Ed*. Van Nostrand Reinhold.

MATHIEU, J. & SCOTT, J. (2000). *An Introduction to Turbulent Flow.* Cambridge University Press.

MILEY, S.J. (1982). *A Catalog of Low Reynolds Number Airfoil Data for Wind Turbine Applications.* Department of Aerospace Engineering, Texas A&M University, Texas, 77843.

NEZU, I (2005). Open-Channel Flow Turbulence and its Research Prospect in the 21st Century. *Journal of Hydraulic Engineering.*

PRANDTL, L. & TIETJENS, O.G. (1934). *Fundamentals of Hydro- and Aeromechanics.* Dover.

SCHLICHTING, H. & GERSTEN, K. (2000). *Boundary Layer Theory, 8th Ed.* Springer.

THOM, A. (1928). An Investigation of Fluid Flow in Two Dimensions*. British Aero. Res. Council R. & M.* **1194***.*

TAMBURRINO, A & GULLIVER, J. S. (1999). Large Flow Structures in a Turbulent Open-Channel Flow. *Journal of Hydraulic Research*.

VITERNA, L.A. & CORRIGAN, R.D. (1981). *Fixed Pitch Performance of Large Horizontal Axis Wind Turbines.* Tech. Rep. CP-2230, NASA.

WHELAN, J. I., GRAHAM, J. M. R. & PEIRÒ, J. (2009). A free-surface and blockage correction for tidal turbines. *Journal of Fluid Mechanics,* 624, 281–291.

WHELAN, J., THOMSON, M. & RAWLINSON-SMITH, R. (2010). Arguments For Modifying The Model Scale Rotor Geometry, 104330/BT/01. *Garrad Hassan & Partners Ltd., St Vincent's Works, Silverthorne Lane, Bristol, BS2 0QD, UK.*

WHELAN, J. (2010). GH Rotor Design – WG4 WP1 D1, 104330/BT/02. *Garrad Hassan & Partners Ltd., St Vincent's Works, Silverthorne Lane, Bristol, BS2 0QD, UK.*

WILLIAMSON, C. H. K. (1996). Vortex Dynamics in the Cylinder Wake. *Annual Review of Fluid Mechanics,* **28**, 477 – 539.

ZDRAVKOVICH, M. M. (1997). *Flow Around Circular Cylinders. Volume 1: Fundamentals.* Oxford University Press.